BELISA
BELGIAN PRINCESS ELISABETH STATION

FINAL REPORT

BELGIAN ICE SHEET-SHELF ICE MEASUREMENTS IN ANTARCTICA

"BELISSIMA"

EA/11/3A

Promotors

Frank Pattyn (Université Libre de Bruxelles, CP160/03, Av. F.D. Roosevelt 50, B-1050 Brussels)
Jean-Louis Tison (Université Libre de Bruxelles, CP160/03, Av. F.D. Roosevelt 50, B-1050 Brussels)

Authors

Frank Pattyn (ULB)
Jean-Louis Tison (ULB)
Denis Callens (ULB)
Kenichi Matsuoka (Norwegian Polar Institute)
Bryn Hubbard (Aberystwyth University)
Reinhard Drews (ULB)
Marie Dierckx (ULB)
Mathieu Depoorter (ULB, University of Bristol)
Morgane Philippe (ULB)

ULB

Table of Contents

SUMMARY

A.   Context

Ice sheets that are in contact with the ocean are highly sensitive to processes occurring at and near the grounding line (Nick et al., 2009; Dupont et al., 2005; Pattyn et al., 2006; Schoof, 2007). The synchronous response of several independent glaciers, coupled with rapid thinning of their floating termini (Shepherd et al., 2004), is generally taken as an indicator that the changes are being forced by the ocean, which has been confirmed recently through sub-shelf observations of Pine Island Glacier (Jenkins et al., 2010). Warming of the waters on the Amundsen Sea continental shelf has led to an increase in the rate of melting at the base of the floating ice shelves (Payne et al., 2007, Jenkins et al., 2010). The resultant thinning of the ice shelves has reduced the longitudinal stresses transmitted upstream allowing more rapid ice flow (Payne et al., 2004). Field evidence and theory indicate that improved understanding of interactions between the ocean and ice and the coupling far upstream with inland ice is needed to assess the response of Antarctic ice sheet to a warming world.

East Antarctic outlet glaciers also show signs of accelerated mass loss (Rignot et al., 2008). The processes involved are likely similar to those operating on the West Antarctic ice sheet, as sub-shelf melting occurs near the grounding lines of many of the major outlet glaciers in Antarctica (Rignot and Jacobs, 2002). The close proximity of the ice shelf to the margin of the continental shelf in many places around Antarctica opens the possibility that relatively warm water originating from the abyssal planes (Circumpolar Deep Water, CDW) could circulate under the shelf and cause enhanced sub-shelf melting (Smedsrud et al., 2006; Payne et al., 2007, Holland et al., 2008, Jenkins et al., 2010). Such enhanced melting may lead to ice shelf thinning, loss of buttressing and provoke grounding line retreat, leading to enhanced ice discharge and enhanced thinning upstream due to stress transmission (Payne et al., 2004; Pattyn et al., 2006). For outlet glaciers characterized by a downsloping bed towards the interior of the ice sheet, such a positive feedback may eventually lead to ice sheet instability (Weertman, 1974; Schoof, 2007). Although a lot of progress has been made on the theoretical level of understanding marine ice sheet stability (e.g. Schoof, 2007), major uncertainties remain linked to the actual response of ice sheets and glaciers to such sub-shelf melting.

However, the interaction with CDW not only leads to sub-ice melting close or at the grounding line, freezing processes (marine ice formation and ice-mélange accretion) are common as well. Both factors establish the basal mass balance of Antarctic ice shelves. Marine ice has been known since the early 1970's. Gow and Epstein (1972) demonstrated for the first time the occurrence of refrozen sea water under the Koettlitz Glacier tongue, near McMurdo Sound in the Ross Sea, Antarctica. Morgan (1972) reported the occurrence of 158 m of ice with very distinct physical and chemical properties under 270 m of continental ice at Amery Ice Shelf. This marine ice (Oerter et al., 1992) shows $\delta^{18}O$ values close to +2‰, proving that it has been formed by freezing sea water. Bulk salinity of marine ice varies between 0.03 and 0.3, which is two orders of magnitude more than continental ice and one to two orders of magnitude lower than sea ice. This puzzling property of ice formed from sea water is yet not fully understood (Eicken et al.,1994; Tison et al. 2001).
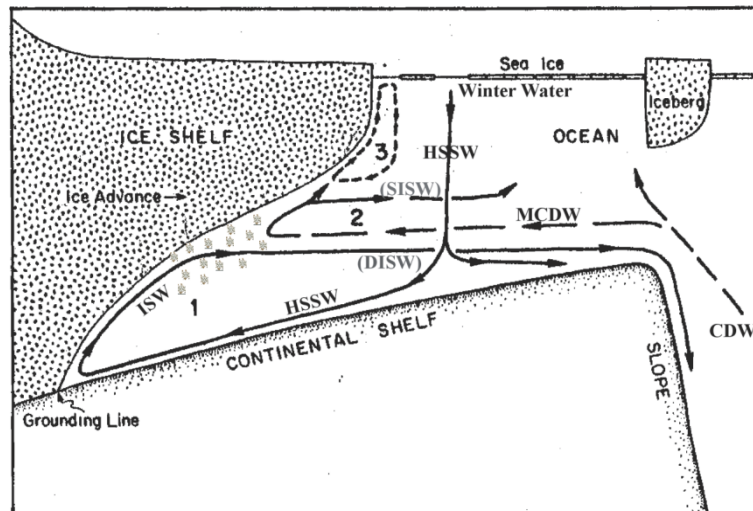
Figure 1: Ocean circulation patterns in the vicinity of ice shelves (Jacobs et al., 1992). HSSW: High Salinity Shelf Water; ISW: Ice Shelf Water; CDW: Circumpolar Deep Water. 1 = Deep Thermohaline Circulation; 2 = Shallow Thermohaline circulation; 3: Summer circulation

Robin (1979) linked marine ice formation to water masses circulation under and in front of the Amery Ice Shelf. Lewis and Perkins (1986) introduced the concept of "ice pump" to describe the overall process summarized in Figure 1 (Jacobs et al.,1992), sometimes called "Deep Thermohaline Circulation" (DTC). Briefly, sea ice formation reject salts in the underlying water and increases its density. This High Salinity Shelf Water (HSSW) sinks and part of it penetrates the sub-ice shelf cavity. The adiabatic descent maintains the water temperature close to the surface melting point (-1.9°C). As it eventually reaches the grounding line of the ice shelf, melting occurs by the lowering of the melting point with pressure. The resulting mix of melt water and HSSW forms a less dense water mass called Ice Shelf Water (ISW) that tends to return to the ice shelf front along the sub-ice shelf cavity ceiling. This leads to nucleation of individual frazil ice crystals through supercooling, which accumulate in bottom crevasses, inverted cavities and between individual ice streams (Corr et al, 1995). Consolidation into marine ice is then slowly driven by heat conduction through the ice shelf ice.

Marine ice formation process has been modelled (Jenkins and Bombosch, 1995; Jenkins and Doake, 1991) and incorporated into regional 3-D ocean circulation models (Holland et al., 2003; Nalker and Holland, 2007; Grosfeld, 1998). Nicholls (1997) discussed observed seasonal variability of water mass properties under the Ronne Ice Shelf in terms of potential impact of reduced sea ice cover under a warming climate. They argue that reduced sea ice cover weakens HSSW production hence continental ice melting at the grounding line and, as a consequence favour stabilization of the ice shelf. However, this implies neglecting the associated reduction of marine ice production, leading to a reduction in ice shelf stability. This balance between melting and refreezing is pivotal in understanding present-day observed changes such as ice-shelf collapse, grounding line retreat or glacier acceleration. For example, it is likely that un-welded crevasse traces remain predilection locations for iceberg calving (Glasser and Scambos, 2008). When accreting in open rifts, marine ice can often be mixed with fallen meteoric ice blocks, sea ice and blown snow to form what is known as the "ice mélange". Depending on the proportion of these various compounds, rheological properties will

be different, which may explain differences in iceberg calving and ice-shelf collapse between different shelves.

B.   Objectives

The BELISSIMA (Belgian Ice Sheet – Shelf Ice Measurements in Antarctica) project focuses on the investigation of the stability of the ice sheet in coastal Dronning Maud Land (DML), East Antarctica, since the last deglaciation. Little is known on how the ice sheet is currently reacting to changes in the environment. Evidence from West Antarctica shows that interaction of the ocean with the ice sheet plays a determining role in the observed thinning, glacier acceleration and grounding-line retreat of the continental ice sheet. Increased melting under the ice shelf leads to decreased buttressing (the ice shelf loses contact with pinning points which slow down the flow), leading to an increased outflow and a positive contribution to sea-level rise.

The objectives are twofold: i) to investigate stability of ice rises (points where the ice shelf gets buttressed), and – more importantly – (ii) to investigate the role of ice-ocean interactions in the stability of the ice sheet/ice shelf system. The project is within the framework of the newly established Princess Elisabeth Station (Antarctica) and the studied area is situated on the coastal stretch (Princess Ragnhild Coast, Dronning Maud Land), 180 km north from the research station, where a number of distinct ice rises have been identified.

BELISSIMA therefore aims to answer the following questions:

1. Are ice rises stable features over the last thousands of years?

2. Is the ice sheet stable in contact with the ocean?

3. Is there an active Deep Thermohaline Convection under the Roi Baudouin Ice Shelf, characterized by sub-ice melting at the grounding line?

4. Is there evidence of marine ice accretion under the ice shelf?

5. What forms the "ice mélange" observed within major rifts in ice shelves?

6. What are the rheological properties of this ice mélange and how do they control the stability of the ice shelf / ice sheet system?

This project investigated a small ice rise at 71°S, 24°E near the DML (Dronning Maud Land) and its immediate surroundings. This 30 km wide ice rise has a distinct flow divide, with ice discharge into shelves located either side of it.

A combined radio-echo sounding survey with differential GPS was performed to examine present basal conditions of the ice rise by subtracting the effects of the radio-wave attenuation from the echo intensity associated with the bed. Temporal variations in the spatial accumulation pattern are retrieved for the past 500 years using shallow radar layers and dated using the shallow firn cores collected in the field. Study of ice flow physics, such as higher order effects, and ice/ocean interaction near grounding

lines is performed using radar layers. Melting and refreezing patterns at the grounding line were inferred this way.

Focus is also placed on the dynamics of the ice shelf close to the grounding line and in nearby rifts, to investigate links between the formation of what is often referred to as the "ice mélange" in crevasses and fractures and the stability of the ice shelf, particularly with respect to sub-ice–ocean interactions. Marine ice and the "ice mélange" in the vicinity of the grounding line is analysed to investigate the role of these inclusions in the stability of the ice-sheet ice-shelf system.

A series of CTD measurements were performed all along the ice shelf front and within different rift systems in the ice shelf that allowed for an easy access to the underlying waters. Such measurements are crucial in understanding the different water masses occupying the continental shelf underneath the floating ice shelf in relation with deeper waters off the continental platform.

Due to the combined expertise in radar methods, ice core analysis, ocean CTD profiling and ice-flow modelling, this project brings along new insights into the presence of a thermohaline circulation underneath the ice shelf. This is likely caused by the potential combined effect of an upwelling of warmer Circumpolar Deep Water (CDW) onto the continental shelf and the formation of dense high-salinity shelf water (HSSW) through sea-ice formation. CDW and/or HSSW may reach up to the grounding line penetrating up to the sub-shelf cavity, where melting occurs due to its higher temperature. The circulation is then completed by the freeze on of a mix of HSSW and ice shelf meltwater (ISW- marine ice formation) in bottom crevasses underneath the ice shelf. Deformation experiments have also demonstrated that marine ice freeze-on has a stabilizing effect on ice shelf dynamics.

Lastly, we investigated the stability of the ice sheet in contact with the ocean. First through an analysis of radar data of major outlet glaciers that are discharging into the ice shelf, and secondly through the analysis of the Raymond effect at the central part of the major ice rise in the Roi Baudouin ice shelf, i.e., the Derwael Ice Rise.

C.   Conclusions

The melting of continental ice (glaciers, ice caps and ice sheets) is a substantial source of current sea-level rise, and one that is accelerating more rapidly than was predicted even a few years ago. Indeed, the most recent report from Intergovernmental Panel on Climate Change (IPCC) highlighted that the uncertainty in projections of future sea-level rise is dominated by uncertainty concerning continental ice, and that understanding of the key processes that will lead to loss of continental ice must be improved before reliable projections of sea-level rise can be produced. Major uncertainties, however, remain on the level of the contribution of the Antarctic ice sheet to sea-level change. Current numerical models project a negative contribution of the Antarctic ice sheet to sea-level rise, due to increased accumulation rates, while satellite remote sensing measures a significant ice loss, through major outlet glaciers of the Antarctic ice sheet.

Ice-penetrating radar and kinematic GPS surveys across a grounding line, and ice core drilling within a zone of rifting farther downstream reveal sub-ice shelf melting near the

grounding line and limited accretion of marine ice in the rift zone. The rate of sub-ice shelf melting is 0.15 m/a, which is rather low for an Antarctic ice shelf. Marine ice accretion is found in a rift system close to the edge of the ice shelf where it is either formed locally or protected from melting due to warmer surface waters near the shelf edge. We conclude that the weak melt rates at the grounding line are not sufficient to sustain large-scale accretion of marine ice. We suspect that similar weak melting/refreezing conditions occur along much of the coastal sector in Dronning Maud Land where ice shelves are interspersed by ice rises and where rifting commonly occurs between those ice rises and the shelf front.

However, CTD measurements along the whole coastal section showed the first evidence in East Antarctica that warm modified circumpolar deep water (mCDW) accesses the grounding line of the East Antarctic Ice Sheet (through a deep trough in the continental shelf). This warmest mCDW water, more than 1.7 degrees warmer than the in-situ freezing temperature, was found at depths similar to the grounding line depth, so it potentially enhances sub-shelf melting near the grounding line of Western Ragnhild Glacier, one of the most distinct fast-flowing glaciers in Dronning Maud Land. Western Ragnhild Glacier is grounded well below sea level with a bedrock slope that is close to zero, potentially facilitating inland grounding-line retreat in response to oceanic perturbations. The current relatively slow flow velocity at the grounding line of 300 m/year is due to an important buttressing effect of two ice rises pinning the ice shelf. Increased melting and subsequent unpinning could lead to rapid, significant grounding line retreat and ice mass loss.

D. Contribution of the project in a context of scientific support to a sustainable development policy

The BELISSIMA project aimed at investigating the processes occurring at the interface between the ice sheet, ice shelf and the ocean and to quantify mass changes in this area.

The main contribution of the BELISSIMA project to a sustainable development policy is that it has played a crucial role in keeping an original Belgian glaciological research capacity operational on both the national and international scale. The teams that participated in BELISSIMA possess at the one hand a unique expertise in glaciological modelling, evident in their state-of-the-art ice flow models and on the other hand a unique expertise in investigating multi-parametric properties of ice and its contact with the ocean. Results and development work performed within this project therefore have found its way in international policy-oriented bodies (IPCC, SCAR, CliC) and have contributed to EU FP7 research projects such as ice2sea (estimating the future contribution of continental ice to sea-level rise).

E. Keywords

Ice sheet – ocean interaction, ice shelf, Circumpolar deep water, radio-echo sounding, marine ice, ice-core drilling

1. INTRODUCTION

Marine ice sheets that terminate in the ocean are particularly sensitive to perturbations at the grounding line (Weertman, 1974; Dupont and Alley, 2005; Pattyn et al., 2006; Schoof, 2007; Gagliardini et al., 2010). Sub-shelf melting occurs near the grounding lines of many of the major outlet glaciers throughout Antarctica (Rignot and Jacobs, 2002; Pritchard et al., 2012). High melt rates underneath ice shelves have been measured in both West Antarctica (Payne et al, 2007; Thoma et al., 2008; Jenkins et al., 2010), and East Antarctica (Smedsrud et al., 2006, Nichols et al., 2006; 2008). Observations of synchronous rapid thinning of the floating termini of several glaciers in a region are generally taken to be an indication that the changes are being forced by the ocean (Shepherd et al., 2004; Thoma et al., 2008). Such forcing leads to increased discharge of inland ice across the grounding line (Schoof, 2007; Rignot et al., 2008; Pritchard et al., 2012). Sub-shelf melting near grounding lines is linked to patterns of large-scale water circulation (Lewis and Perkins, 1986; Jacobs et al., 1992; Holland, 2008). Sub-shelf melt rates are relatively high when Circumpolar Deep Water (CDW) reaches the continental shelf, and generally lower when sea ice formation results in high salinity shelf water (HSSW). Melting and freezing along the shelf interface are part of the ``ice pump'' that is controlled in part by the intensity of HSSW circulation (Lewis and Perkins, 1986).

However, the most common water mass over the narrow continental shelves of East Antarctica is the Antarctic Surface Water (ASW; Withworth et al., 1998). At the coast this surface layer deepens as a result of downwelling forced by the easterly winds blowing along the coast. Where the ice sheet topography is steep and the continental shelf narrow (i.e. around East Antarctica) the downwelling is so effective that the whole of the water column over the continental shelf is comprised of ASW (Nøst et al., 2012). Similar to HSSW, this cold ASW can also melt the ice shelf base (Hattermann et al., 2012), producing Ice Shelf Water (ISW). This ISW, derived from melting meteoric ice and mixing with HSSW/ASW, is also an important component of the ocean circulation. It is known that ISW production varies for different ice shelves but relative contributions from HSSW and CDW are not known for much of East Antarctica.

Most of the evidence for ice-ocean interactions comes from the large Antarctic ice shelves or from ice shelves of the West Antarctic Ice Sheet, but apart from studies on Fimbul ice shelf (Nicholls et al., 2006; 2008; Hattermann et al., 2012), little is known about the ice shelves in the Dronning Maud Land (DML) sector of East Antarctica, although most of the DML coast is characterized by marine-terminating glaciers in ice shelves. The Antarctic coastline between 10°W and 40°E is characterized by fringing ice shelves supplied by outlet glaciers of the coastal mountain ranges in this region. Few of these outlet glaciers have high flow speeds due to ice shelf buttressing and typically small drainage areas, thus this area has often been overlooked in studies investigating ice shelves' roles in ice sheet mass balance (Rignot and Jacobs, 2002). Oceanographic observations on or near this portion of the East Antarctic continental shelf are very rare, and repeat sections have typically only been collected in locations corresponding with ship access to research stations. The continental shelf is quite shallow where it has been observed in this region (typically 200-300 m deep at its northern margin (Nøst et al., 2011; Timmermann et al., 2010)), and the presence of the Weddell Gyre offshore has been assumed to aid in separating this coastline from the warm Circumpolar Deep

Water (CDW) that follows the path of the Antarctic Circumpolar Current offshore (Orsi et al., 1995).

Herein, we combine several empirical lines of evidence to investigate the nature of sub-shelf circulation beneath an ice shelf on the Princess Ragnhild Coast, i.e., Roi Baudouin Ice Shelf (RBIS), DML, East Antarctica. We use ice-penetrating radar, GPS measurements ,ice core drilling and oceanographic CTD profiles to investigate ice-ocean interactions on RBIS. Comparison of observed radar-detected englacial reflectors with results from an ice flow model is used to infer basal melting across the grounding line. Direct evidence of sub-shelf marine ice accretion comes from four ice cores drilled through the shelf. Furthermore, we show the first evidence in East Antarctica that warm modified circumpolar deep water (mCDW) accesses the grounding line of the East Antarctic Ice Sheet (EAIS) through a deep trough in the continental shelf, based on CTD (Conductivity, Temperature, Depth) measurements. The warmest mCDW water, more than 1.7 degrees warmer than the in-situ freezing temperature, was found at depths similar to the grounding line depth, so it potentially enhances sub-shelf melting near the grounding line of Western Ragnhild Glacier, one of the most distinct fast-flowing glaciers in Dronning Maud Land (Rignot et al., 2011).

2. METHODOLOGY AND RESULTS

Study area

During the Austral summer 2008-09, we conducted field work in the vicinity of a small ice-rise promontory in RBIS, East Antarctica. Surface topography shows that the ice-rise promontory has a local flow pattern (Figure 2). Downstream of the promontory, a large rift system ∼ 5 km from the ice shelf edge has a maximum width of 2 km and is filled
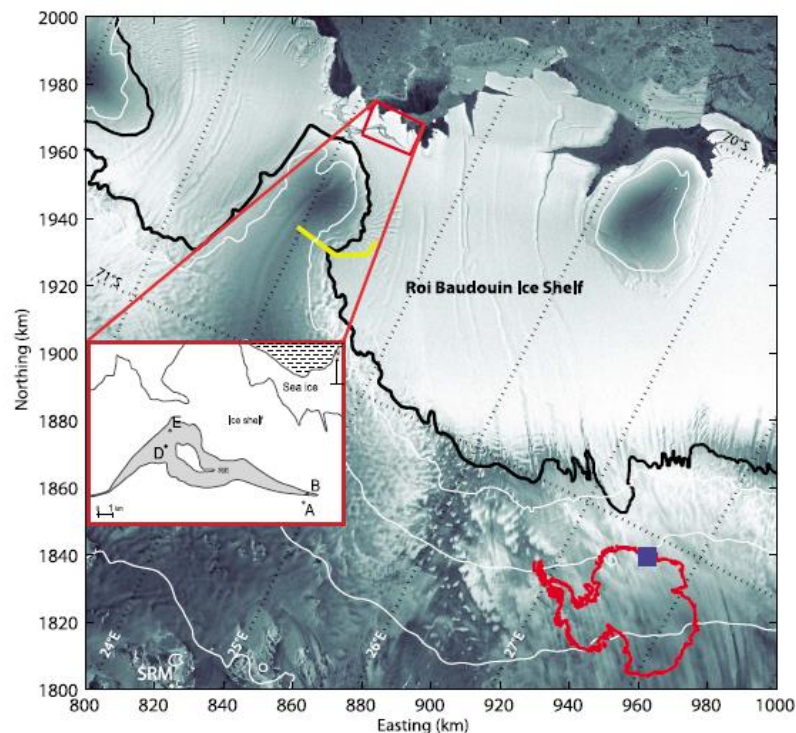
Figure 2: Location of the ice-rise promontory and the Roi Baudouin Ice Shelf (RBIS), Dronning Maud Land, East Antarctica. Contour lines are in white (contour interval is 300 m, starting at 200 m a.s.l.; Bamber et al., 2009). The grounding line is given in black (Bindschadler et al., 2011). The yellow line is the radar traverse. Locations of the 2008-2009 boreholes in the rift are shown in the inset figure. RAMP (Radarsat) is used as a background image. SRM = Sør Rondane Mountains.

with well consolidated ``ice mélange''. The bathymetry beneath the ice shelf is relatively shallow; it is 200-300 m b.s.l. near the shelf front (Nishio et al., 1984), and it approaches 500 m b.s.l. near the grounding line (Nishio et al., 1984; Timmermann et al., 2010). In view of our measured ice thickness, water column thickness beneath the shelf varies between 0 and 200 m. The ice velocity in this area is several tens of meters per year, but reaches values up to 350 m/a in the central part of RBIS, further to the east of our study area (Rignot et al., 2011).
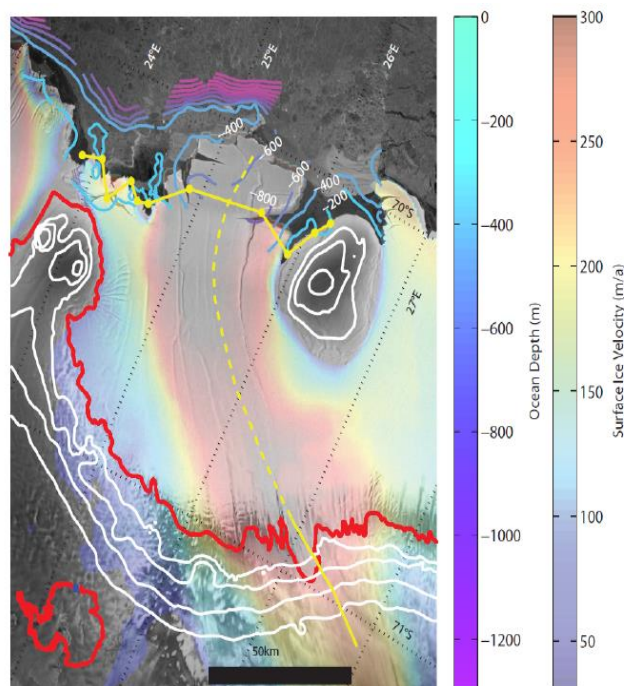

Figure 3: Overview of the study area. Interferometric velocities are from Rignot et al. (2011), surface topography from Bamber et al. (2009), and bathymetry from Derwael (1965). The grounding line is shown in red (24). Oceanographic measurements were made in December 2011 using a Seabird Electronics SBE19+ CTD instrument equipped with a supplemental dissolved oxygen sensor, at sites (yellow dots) for which results are displayed in Figure 7. Cast 12, the location of the mCDW measurements, is just to the East of the dashed central flowline. The pale green line paralleling the ice flow direction is the position of Figure 8 (dashed/solid), which shows the radar tracks (solid) from which grounding-line ice thickness of the Western Ragnhild Glacier was inferred.

During the Austral summer of 2010-2011 and 2011-2012, field activities extended further towards the East, i.e. across the whole RBIS up to Derwael ice rise (Figure 3). Contrary to the ice-rise promontory bordering the Western part of RBIS, this ice rise sticks out within the ice shelf as a local ice island covered with a grounded ice sheet and exhibiting a local (radial) ice flow pattern.

Field measurements

Ice-penetrating radar and GPS profiling

We collected ice-penetrating radar profiles across the ice-rise promontory, the ice shelf and the Derwael ice rise (Figures 2 and 3), using a 5-MHz impulse radar system (Matsuoka et al., 2012). The transmitter and receiver were separated by 45 m and towed in line. Each record consists of several hundred stacked (averaged) waveforms to improve the signal to noise ratio. Additional processing includes bandpass filtering,

corrections for surface topography and conversion of two way travel time to depth. We assume the wave speed in ice is 169 m/μs. Uncertainty in thickness comes from uncertainty in the wave speed (about 2 m/μs) and from picking the two-way travel time from the surface to the bed. The former corresponds to 1.2% of the ice thickness and the latter is about 0.1 μs for 5 MHz, which corresponds to ~8.5 m. Assuming the errors are uncorrelated, total uncertainty on the ice-rise promontory (<600 m thick) is up to ~11 m. On the ice shelf (~250 m thick), total uncertainty is ~9 m.

Radar profiles show both reflections from the bed and englacial reflectors. Ice thickness is ~600 m between the crest of the ice-rise promontory and the grounding line (Figure 4). Downstream from the grounding line on the ice shelf, ice thickness decreases rapidly to ~250m. At some locations on the shelf, clutter from multiple hyperbolic echoes beneath surface rumples hampered detection of the basal interface. In previous work we found an abrupt increase in basal reflectivity (near km 13), which is within a kilometre of where the shelf is freely floating (Matsuoka et al., 2012). The magnitude of this reflectivity change is consistent with a change from a grounded (possibly wet) environment to an ice-ocean interface (Matsuoka et al., 2012).
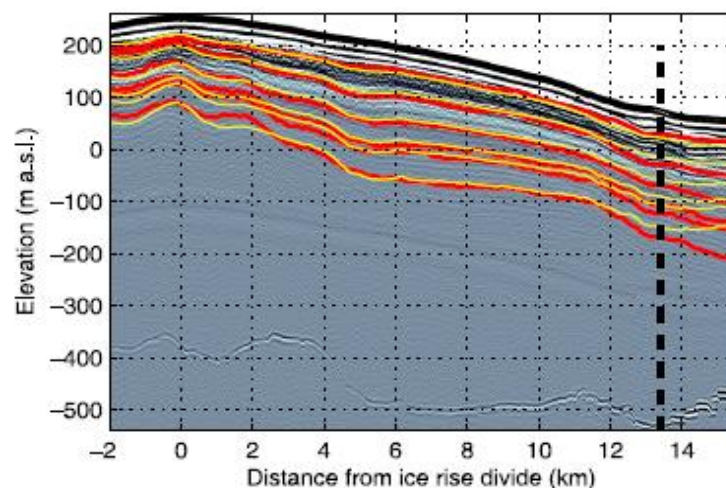

Figure 4: Section of radar profile (location shown in Figure 2) across the ice-rise promontory and the grounding line (vertical dashed line). Comparison of radar detected reflectors (red), and modelled isochrones (yellow) for the standard experiment (no basal melting) shows large mismatch at the grounding line and within the ice shelf; the mismatches for different model runs are shown in Figure 7.

Profiles were positioned using a roving Leica SR20 differential GPS (L1) referenced to a base station located on the grounded ice-rise promontory. The absolute position of the base station on the ice-rise promontory was obtained from Precise Point Processing, and further adjusted to the EGM96 geoid model to obtain a position relative to mean sea level. The EGM96 model has a discrepancy of 0.27 m compared to measured geoid heights in Breid Bay, near our field site (Shibuya et al., 1999). A tide model (Padman et al., 2002) was employed to further correct elevations of the roving station on the ice shelf. The tide model predicts tidal amplitudes of less than 1.6 m, with changes of less than 0.4 m predicted over the 5-hour period of our radar and GPS measurements across the ice shelf. Horizontal and vertical position errors for the roving GPS are of the order

of 0.1-0.2 m (Pattyn et al., 2010). For subsequent analyses, we prescribed the grounding line to be the position where the ice becomes freely floating.

Ice-core drilling

To study the surface ice shelf structure and detect the presence of marine ice in the rift, 13 boreholes (with retrieved ice cores) between 5 and 66 m long were drilled north of the ice-rise promontory using either an Eclipse or a SIPRE-based[1] electro-mechanical drill in 2008-2009 and 2010-2011 (Figure 2 and 5, Table 1): (i) on the ice shelf (cores 08-S1 [A in Figure 2] and 10-S1); (ii) on the slope entering the apex of the rift (core 08-T1 [B in Figure 2]); (iii) within the rift system (cores 08-R1, 08-R2 [D in Figure 2], 08-R3 [E in Figure 2] and 10-R1 to 10-R6). Core samples were generally analysed at 0.5-1.0 m depth intervals for their isotopic composition ($\delta^{18}O$, δD), bulk density, salinity and ice texture. Bulk salinity was measured according to standard procedure (Khazendar et al., 2001), with precision of ± 0.05 psu. Bulk density was measured using the mass/volume technique (± 0.05 precision) and cross-calibrated against X-Ray tomography (see below). Isotopic measurements were made using a Thermo-Finnigan Mass Spectrometer Delta Advantage $\delta^{18}O$ $\pm$ 0.05‰, δD $\pm$ 1.00‰). On core A (08-S1), samples of isotopes and density of the meteoric ice collected at 100 mm resolution (not shown here) reveal a clear seasonal signal. The accumulation rate (0.27 m/a w.e.) derived from these measurements is in accordance with regional mass balance modelling results (van de Berg et al., 2006).

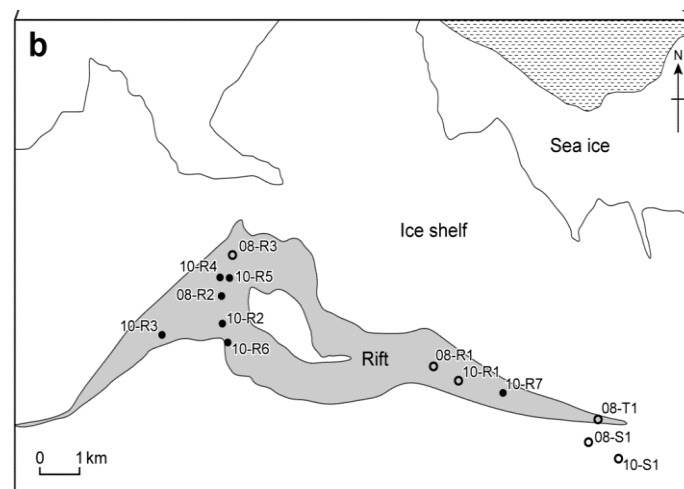**Figure 5**: Location map of the 2008-2009 and 2010-2011 BELISSIMA boreholes. Boreholes logged by OPTV are represented as open circles.

---

[1] The Eclipse drill allows drilling down to several hundred meters, while the SIPRE-type drill is more portable and specially equipped for drilling into water saturated permeable ice, such as ice shelf ice and rift ice would be. Both were used in the field.

A digital optical televiewer (OPTV - Hubbard et al., 2008; 2012) was deployed in some of the boreholes (open circles in Figure 5). .Logging by OPTV has the potential to provide important information in terms of identifying and characterizing the ice types intersected. OPTV differs in one fundamental respect from traditional (directional)

Table 1. Summary data for boreholes cored on the RBIS in 2008 and 2010

Borehole	Location	Northing*	Easting*	Length m	OPTV	Note
08-S1	Shelf	70 21 40.7	24 27 11.3	15.24	Yes	Terminated englacially in water-saturated firn
08-T1	Rift tip	70 21 25.0	24 27 33.0	38.28	Yes	Terminated englacially in firn
08-R1	Rift	70 21 14.5	24 25 37.6	9.65	Yes	Terminated englacially in water-saturated ice
08-R2	Rift	70 20 12.5	24 13 09.2	18.40	No	Penetrated rift base into platelet ice/cavity
08-R3	Rift	70 19 28.6	24 13 22.4	13.26	Yes	Penetrated rift base into platelet ice/cavity
10-S1	Shelf	70 21 38.9	24 27 14.9	66.40	Yes	Terminated englacially in ice-shelf ice
10-R1	Rift	70 20 44.4	24 21 07.8	13.56	Yes	Penetrated rift base into platelet ice/cavity
10-R2	Rift	70 20 05.6	24 12 06.2	7.29	No	Penetrated rift base into platelet ice/cavity
10-R3	Rift	70 20 13.8	24 09 48.1	29.71	No	Penetrated rift base into platelet ice/cavity
10-R4	Rift	70 19 32.3	24 12 00.0	19.19	No	Terminated englacially in water-saturated rift ice
10-R5	Rift	70 19 32.3	24 12 21.3	21.44	No	Terminated englacially in water-saturated rift ice
10-R6	Rift	70 20 20.1	24 12 11.9	4.86	No	Penetrated rift base into platelet ice/cavity
10-R7	Rift	70 20 53.2	24 22 49.4	11.02	No	Terminated englacially in water-saturated rift ice

*These locations were recorded at the time of coring. They have since been advected with the motion of the ice shelf, which in this area is moving in an approximately northerly direction by ~ 350–$380 \, \mathrm{m \, a^{-1}}$ (Pattyn and others, 2005).

borehole video in that OPTV acquires a geometrically-accurate image of the complete borehole wall. This is achieved by the probe's downward-looking digital camera recording a 360° annular image of the borehole wall as reflected in a hyperboloidal mirror (Figure 6a and b). Accurate winch control then allows the probe to be raised and lowered at a precise rate along the borehole, typically producing images with a vertical resolution that can be user-set to a pixel dimension as small as 1 mm and at a lateral resolution of either 360 or 720 pixels per row (~ 1.0 mm and ~ 0.5 mm per pixel respectively for a borehole of 12 cm diameter). This geometrical accuracy provides a powerful means of mapping the structures that intersect a borehole wall because each visible intersecting plane appears as a sinusoidal trace on the raw OPTV image. Here, the dip and dip-direction of each such plane (orientated by magnetometers located within the OPTV probe) are represented respectively by the amplitude and phase of its associated sinusoid (Figure 6c and d). Structural analysis of an OPTV log thereby allows all such features to be located, characterized in terms of their thickness and appearance, and their orientations to be logged.

OPTV was recently applied for the first time to ice boreholes by Hubbard and others (2008). Subsequently, Roberson and Hubbard (2010) applied the technique to an array of boreholes drilled by hot water at Midre Lovénbreen, Svalbard, in an attempt to determine the structural composition of this polythermal valley glacier. Here, OPTV logs successfully revealed bubble-rich layers and bubble clouds, debris bands (including individual clasts) and several generations of stratification and folding.
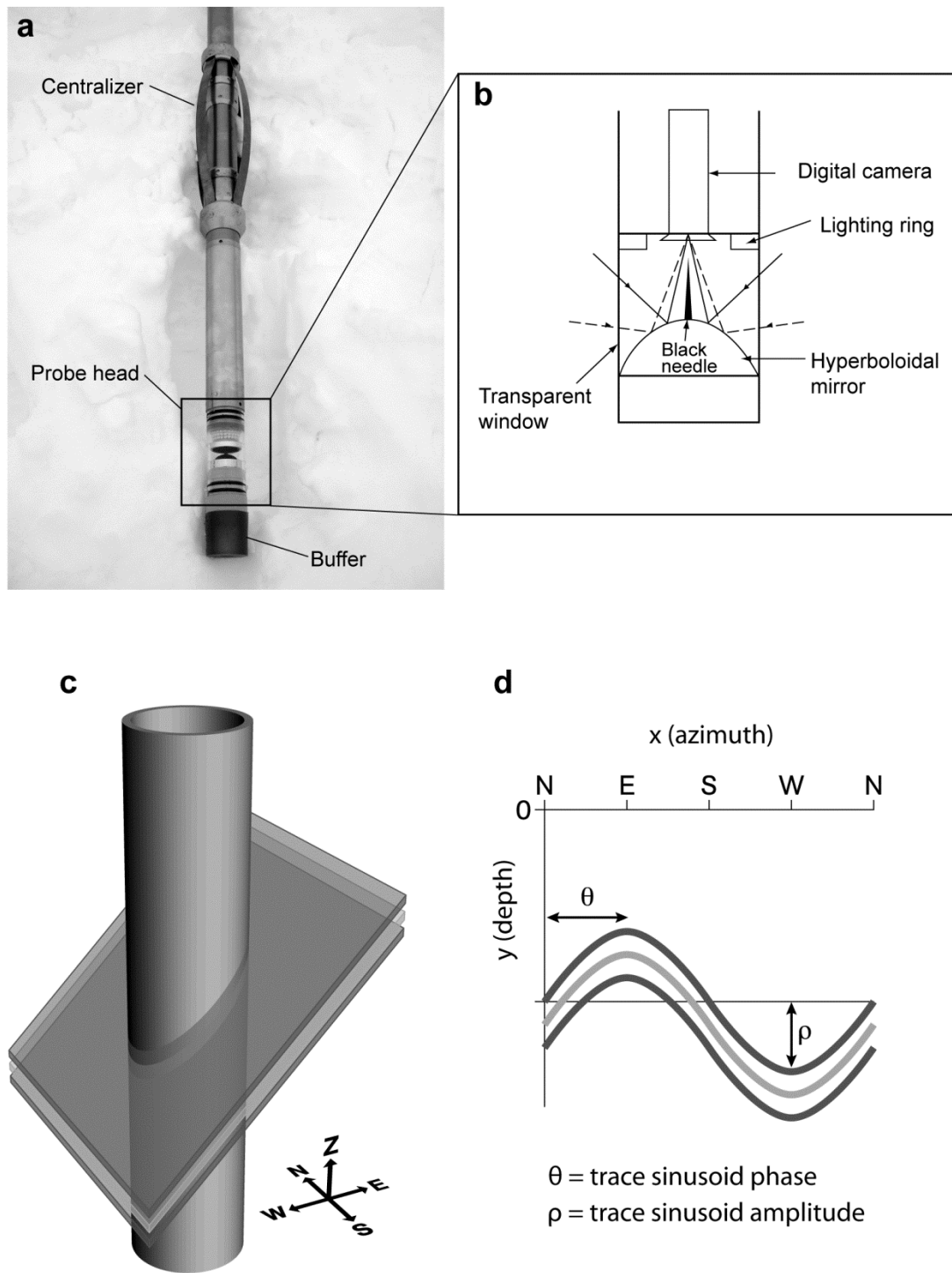
Figure 6: Illustration of the principles of optical televiewer operation. (a) image of OPTV probe and (b) expanded sketch of probe head; (c) schematic illustration of a borehole intersecting three closely-spaced, layers dipping west, and (d) illustration of their equivalent sinusoids on the raw OPTV image.

In this case, where boreholes were drilled by hot water and no core was therefore retrieved, the OPTV analysis was particularly valuable in that it allowed 'virtual' core images to be recreated by rolling the raw (outward-looking) images acquired of the borehole walls and viewing them inwards. OPTV analysis can also potentially provide important complementary information from boreholes from which actual ice core has been recovered. First, OPTV views laterally into the ice surrounding the borehole, thereby providing a deep-field image with the capacity to reveal properties not easily identifiable from (or intersected by) a core that is typically 8-12 cm in diameter. Second, OPTV images cover the entire length (and circumference) of a borehole wall, whereas core may not be retrieved from the borehole's full length, for example being absent from englacial channels or voids. Core sections can also be fractured beyond reconstruction. Third, OPTV imaging can view unconsolidated materials that may not be recoverable as a solid core. This facility may be particularly valuable, for example, in boreholes that intersect unconsolidated honeycomb ice or sub-ice-shelf platelets. Despite this potential, however, OPTV has not yet been applied to ice-shelf boreholes.

Once drilled, OPTV analysis was carried out as soon as possible, and usually within some tens of minutes, in order to avoid borehole closure by freezing and, where boreholes penetrated the cavity, borehole clogging by buoyant platelets rising up the seawater column in the boreholes. The latter effect was unfortunately common, generally occurring within some minutes of the corer being removed from the hole – effectively preventing OPTV logging of several rift boreholes. Once logged, OPTV images were collated, analysed and prepared for presentation (including rolling to create virtual core images) using WellCAD software. This analysis included calculating the luminosity (expressed in non-dimensioned units of RGB pixel brightness) of each 1 mm depth step, represented by the mean value of each ring of 720 pixels. Within some metres (depending on the optical transmissivity of the material being cored) of the borehole surface recorded light is dominated by that transmitted from the surface, but below this zone it is exclusively composed of that reflected back from the borehole walls to the OPTV sensor. Since borehole illumination, achieved by a circular array of white LEDs, is uniform in time, and therefore also in space as the probe moves along a borehole, the net luminosity of the recorded signal varies with the reflectivity of the material forming the borehole wall.

Conductivity – Temperature – Depth (CTD) measurements

Oceanographic measurements were made in December 2011 using a Seabird Electronics SBE19+ CTD (Conductivity – Temperature – Depth) instrument equipped with a supplemental dissolved oxygen sensor. Absolute depth measurements were made using a sonic ranger. An overview of the measurement sites is given in Figure 3.

Ice flow modelling

Model setup

Englacial reflectors detected with 5 MHz radar are principally caused by changes in ice density and acidity (Fujita et al., 1999), and they are generally considered to be isochrones. In this section we generate isochrones using a numerical ice flow model and conduct experiments with different boundary conditions to determine the range of

conditions that minimize the mismatch between the spatial pattern of modelled and measured reflectors.

In regions where radar-detected reflectors are at shallow depths (and given the low ice flow velocities of the grounded ice sheet) the recent spatial pattern of accumulation can be inferred using the local-layer approximation (Haefeli, 1963; Waddington et al., 2007). We scale the local accumulation pattern across the ice-rise promontory using the regional value of 0.27 m/a w.e. (van de Berg et al., 2006).

We use an isothermal higher-order, steady-state ice sheet model (Pattyn, 2002a; 2010), constrained by the local surface mass balance obtained from the local-layer approximation, to reconstruct the age distribution across the ice-rise promontory and shelf. In a Cartesian coordinate system, the horizontal velocity field along a flowline and under plane strain conditions is (Pattyn, 2002a):

$$4\frac{\partial}{\partial x}\left(\eta\frac{\partial u}{\partial x}\right) + \frac{\partial}{\partial z}\left(\eta\frac{\partial u}{\partial z}\right) = \rho g\frac{\partial(b+H)}{\partial x} \tag{1}$$

where u is the horizontal velocity along the flowline, b and H the bottom of the ice and the ice thickness, respectively, and where the effective viscosity η is defined by

$$\eta = \frac{1}{2}A^{-\frac{1}{n}}\left[\left(\frac{\partial u}{\partial x}\right)^2 + \frac{1}{4}\left(\frac{\partial u}{\partial z}\right)^2\right]^{\frac{1-n}{2n}} \tag{2}$$

Here, A and n are the flow parameter and the exponent in Glen's flow law, respectively ($A = 10^{-17}$ Pa^{-n} a^{-1}; $n = 3$). The value of A corresponds to ice with a mean temperature of -10°C, which is consistent with the balance velocities imposed at the boundaries of the domain (see below). At this point, thermomechanical coupling is not considered; the effect of including this coupling on the modelled spatial pattern of isochrones would influence the absolute age of the lower layers, where the highest temperature gradients occur. However, since detected reflectors are restricted to the upper half of the ice column, this effect is therefore limited.

For modelling purposes it is convenient to scale the velocity field in the vertical dimension to the ice thickness. Defining $\zeta = \frac{b+H-z}{H}$, the surface transforms to $\zeta = 0$, while the bottom of the ice mass becomes $\zeta = 1$. The horizontal flow field (1) is therefore rewritten as (Pattyn, 2003):

$$4\frac{\partial}{\partial x}\left(\eta\frac{\partial u}{\partial x} + a_x\eta\frac{\partial u}{\partial\zeta}\right) + 4a_x\frac{\partial}{\partial\zeta}\left(\eta\frac{\partial u}{\partial x} + a_x\eta\frac{\partial u}{\partial\zeta}\right) + \frac{1}{H^2}\frac{\partial}{\partial\zeta}\left(\eta\frac{\partial u}{\partial\zeta}\right) = \rho g\frac{\partial(b+H)}{\partial x} \tag{3}$$

where

$$a_x = \frac{1}{H}\left(\frac{\partial b}{\partial x} + (1-\zeta)\frac{\partial H}{\partial x}\right) \tag{4}$$

while (2) transforms to

$$\eta = \frac{1}{2} A^{-\frac{1}{n}} \left[\left(\eta \frac{\partial u}{\partial x} + a_x \eta \frac{\partial u}{\partial \zeta} \right)^2 + \frac{1}{4H^2} \left(\frac{\partial u}{\partial \zeta} \right)^2 \right]^{\frac{1-n}{2n}}$$

(5)

Boundary conditions for the model are obtained from balance velocities derived by integrating the surface mass balance from the ice divide to the end of the surveyed profile. The velocity at the model domain boundary is then fixed to the balance velocity. Basal velocities are kept zero at the base, except in the ice shelf, where basal friction is set to zero so that velocities at the base equal those at the surface (Pattyn, 2003).

The vertical velocity field is derived from mass conservation combined with the incompressibility condition for ice. Given an ice sheet in steady state, a simple analytical expression can be obtained, based on the horizontal velocity field (Hindmarsh, 1999), i.e.

$$w(x, \zeta) = - \left[\frac{\zeta^{n+2} - 1 + (n + 2)(1 - \zeta)}{n + 1} \right] \dot{a} - \dot{m} + u\nabla b + (1 - \zeta)u\nabla H$$

(6)

where w is the vertical velocity, $\dot{a}$ is the local accumulation rate, and $\dot{m}$ is the basal melting rate. For plug flow (ice shelf), (6) reduces to $w(x, \zeta) = (\zeta - 1)\dot{a} - \zeta\dot{m}$ (Hindmarsh, 1999).

The age calculation within the ice sheet is written as an advection equation with a small diffusion term added in order to stabilize the numerical solution (Huybrechts, 1994; Greve, 1997; Pattyn, 2002b):

$$\frac{\partial \Lambda}{\partial t} = 1 - u\frac{\partial \Lambda}{\partial x} - w\frac{\partial \Lambda}{\partial z} + D_a \frac{\partial^2 \Lambda}{\partial z^2}$$

(7)

where Λ is the ice age (a), and D_a a diffusion coefficient (5 10^{-8} m² a^{-1}) (Mügge et al., 1999). Written in the scaled coordinate system, (7) becomes

$$\frac{\partial \Lambda}{\partial t} = 1 - u\frac{\partial \Lambda}{\partial x} - \left(\frac{w}{H} - a_x \right)\frac{\partial \Lambda}{\partial \zeta} + \frac{D_a}{H^2} \frac{\partial^2 \Lambda}{\partial \zeta^2}$$

(8)

Boundary conditions to this equation are $\Lambda(0) = 0$ at the surface and the age of the integration time at the bottom of the ice mass (typically 10 ka). The choice of this value has no effect on the age of the identified isochrones. The model is solved numerically on a finite-difference grid, equally spaced in x and unequally spaced in ζ, providing a higher resolution approaching the base of the ice mass (Pattyn, 2002a).

Replicating englacial radar reflectors

Based on the inferred accumulation pattern from the shallow radar reflectors, each observed isochrone was dated using a minimization procedure by reducing the mismatch between observed and modelled isochrone depth, leading to ages ranging from 175 to 957 a BP for the uppermost and lowermost isochrones, respectively. This

procedure consists of calculating the misfit between an observed isochrone and a series of modelled isochrones of different age. The smallest misfit then corresponds to the age of the observed isochrone. In general, the model produces a good fit between observed and calculated isochrone depths for the grounded ice sheet profile, except for the area around the grounding line where radar-detected reflectors dip downward (Figure 4).

Causes of downwarped reflectors near the grounding line

This anomaly could be caused by several processes, including subglacial melting at the grounding line or a local increase in surface accumulation, both of which could cause downward motion of the reflectors. Other possible processes could be related to temporal variability in surface accumulation (unlikely since the grounded part would be equally affected by this effect), or to the convergent flow as the flowline turns into the main ice shelf (three-dimensional effects, Figure 2). These are discussed below.

In order to examine possible effects from sub-shelf melting and surface accumulation, we follow the approach of others (e.g. Catania et al., 2006; 2010) and conduct a series of sensitivity experiments using the ice-flow model. We forced the model with anomalies in surface accumulation/ablation (ranging from -0.25 to 0.25 m/a) and basal melting (0 to 0.25 m/a) for the ice shelf (between the grounding line and a distance of 2 km downstream) and calculated the RMS error between observed and calculated isochrone depths (Figure 7). For each experiment shown, we assume that the basal melting and accumulation anomalies are constant through time and spatially distributed over a zone of 2 km. The best fit to the data is obtained with no surface accumulation anomaly and basal melting of 0.15 m/a (Figure 7). Reasonable fits can be obtained with small surface anomalies and slightly lower or higher values of basal melting (0.1 to 0.2 m/a), but all results indicate that basal melting is required.
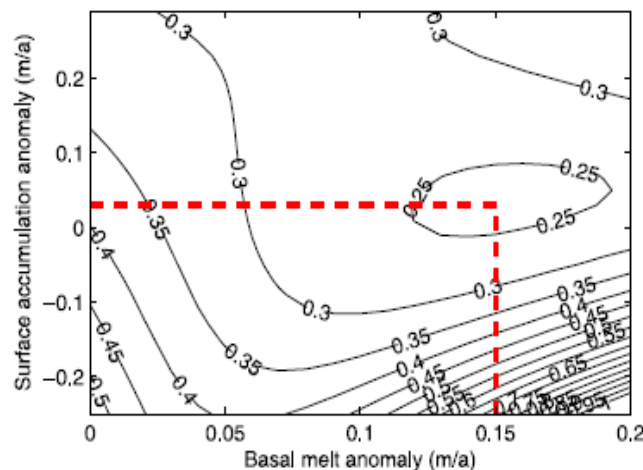

Figure 7: Minimization of the RMS error (m) between observed and modelled isochrones for different combinations of accumulation/ablation and basal melting near the grounding line. The best fit is obtained with basal melting of 15 cm/a and no accumulation anomaly.

The experiments above consider a continuously applied anomaly over a sustained period of time. We therefore tested applying anomalies over shorter time spans as well, but all led to worse misfits. Due to horizontal ice flow, any anomaly is advected downstream, hence the upwarping of the deeper layers at and downstream from the grounding line disappears when the anomaly is applied for any given period in the past.

Conditions of plane strain are valid for the grounded ice flow in the saddle area of the ice-rise promontory (where flowlines are strictly parallel to each other), but do not apply in the ice shelf because of the turning of ice flow (indicated by the flow stripes evident on the ice shelf; Figure 2). In this area, ice flows convergently. Since mass conservation implies that $\nabla \cdot v = 0$, we obtain for a flowline (Reeh, 1998; Pattyn, 2002a):

$$\frac{\partial w}{\partial \zeta} = H\left(\frac{\partial u}{\partial x} + a_x \frac{\partial u}{\partial \zeta}\right) + H\dot{\varepsilon}_{xx} \tag{9}$$

where $\dot{\varepsilon}_{xx} = \frac{\partial v}{\partial y}$ is the transverse strain rate and v the velocity in the y direction. Plug flow of the ice shelf implies that $\frac{\partial w}{\partial \zeta} = \dot{a} - \dot{m}$ and that $\frac{\partial u}{\partial \zeta} = 0$. Under simplified conditions of plane strain, $\dot{\varepsilon}_{xx} = 0$, it is therefore safe to say that

$$H\frac{\partial u}{\partial x} = \dot{a} - \dot{m} \tag{10}$$

However, for convergent flow, $\dot{\varepsilon}_{xx} < 0$, so the vertical velocity gradient $\frac{\partial w}{\partial \zeta}$ is reduced. Since $\frac{\partial w}{\partial \zeta} - \dot{a} = -\dot{m}$, this implies a higher basal melt rate to match the downwarping pattern than that calculated above. Conversely, divergent flow would have the opposite effect (i.e., less basal melt needed to explain the pattern). Although it is difficult to estimate the amount of buttressing due to the convergent flow, we can consider the calculated basal melt anomaly of 0.15 m/a is a lower bound and actual melt rates are likely higher.

Characterization of material facies in the ice shelf and within the ice shelf rift

OPTV as a descriptor of ice shelf firnification processes

The OPTV logs of the two boreholes cored into the ice shelf proper, 08-S1 and 10-S1 (Figure 5; Table 1), reveal similar material properties, with 66 m-long 10-S1 providing the longer record. The log of 10-S1, presented in Figures 8 and 9, has three notable features. First, regularly-repeated dark layers, which have a typical luminosity of ≤ 100 units lower than the local image background, can be observed along most of the length of the core.

The spacing of these layers gradually decreases from ~ 1.0 m near the borehole's upper surface (e.g., five regularly-spaced darker layers between the depths of 4 and 9 m in Figure 8) to ~ 0.15 m near its base (e.g., seven regularly-spaced darker layers between the depths of 51.5 and 52.5 m in Figures 8 and 9b). Although still visible, these layers are more difficult to distinguish from the (now darker) background towards the base of the borehole. Second, sharply-defined very dark layers, typically with a luminosity that is > 100 units lower than the local image background, are observed intermittently along the full length of the borehole. For example, four distinctive dark bands are located at a depth of between 30 and 31 m, each of which is 5-20 cm thick (Figure 8 and 9a). Thus, the luminosity of these layers is typically similar to, or darker than, that of the thinner

and more regular layers noted above. Finally, if both of the above sets of dark layers are removed from the analysis, the background reflected light intensity of the OPTV log of 10-S1 decreases consistently down the borehole, from typical values of ∼400 near the ice-shelf surface to ∼150 at the base of the borehole, visible in both Figure 8 and Figure 9.
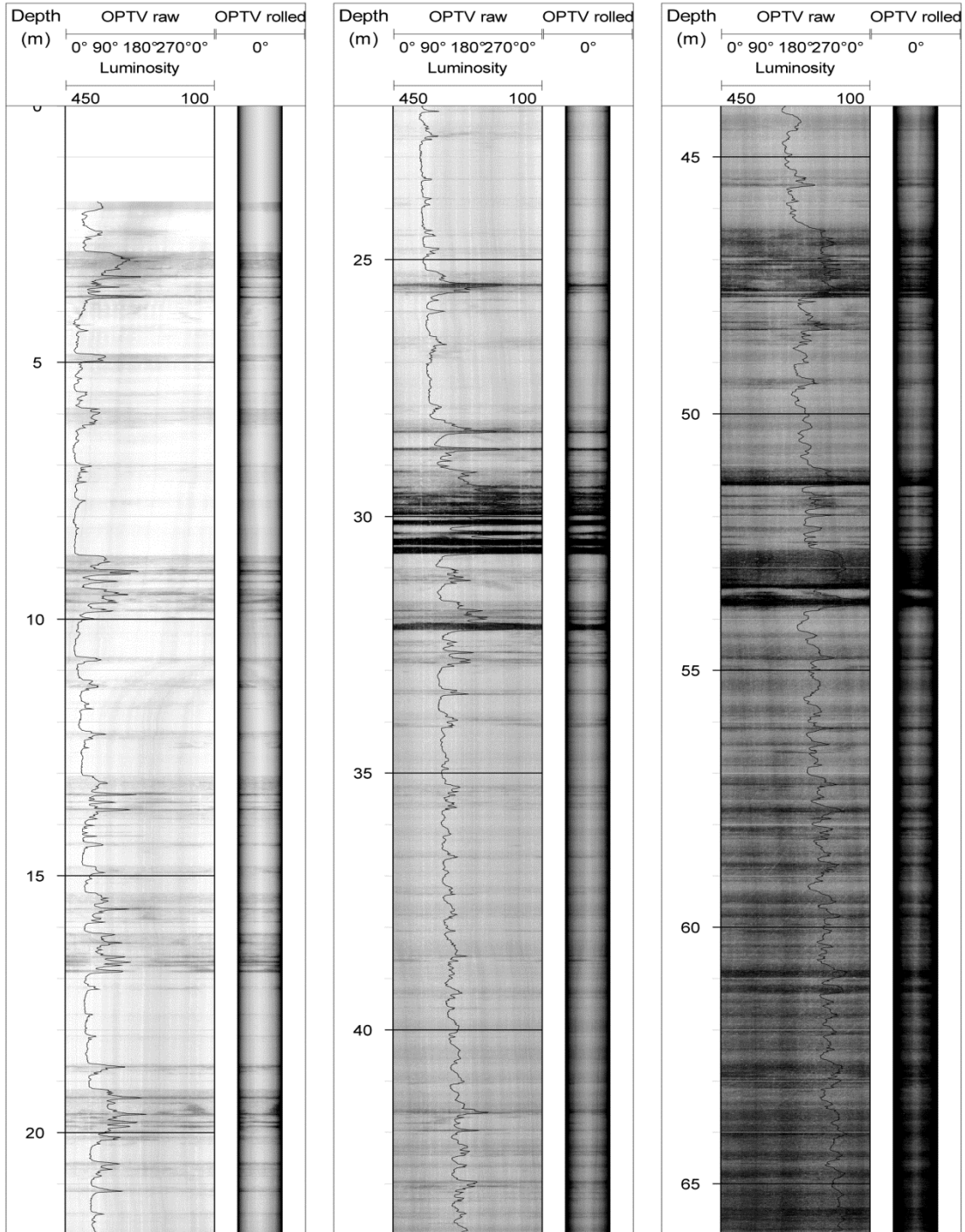

Figure 8: OPTV log of the full length of ice shelf core 10-S1. The raw OPTV image is plotted on the left hand side of each panel and its rolled equivalent is plotted on the right. The luminosity trace overlaid on the raw OPTV image is sampled each millimetre in the vertical and is scaled to decrease, over the range 450-100 (non-dimensioned) units, to the right
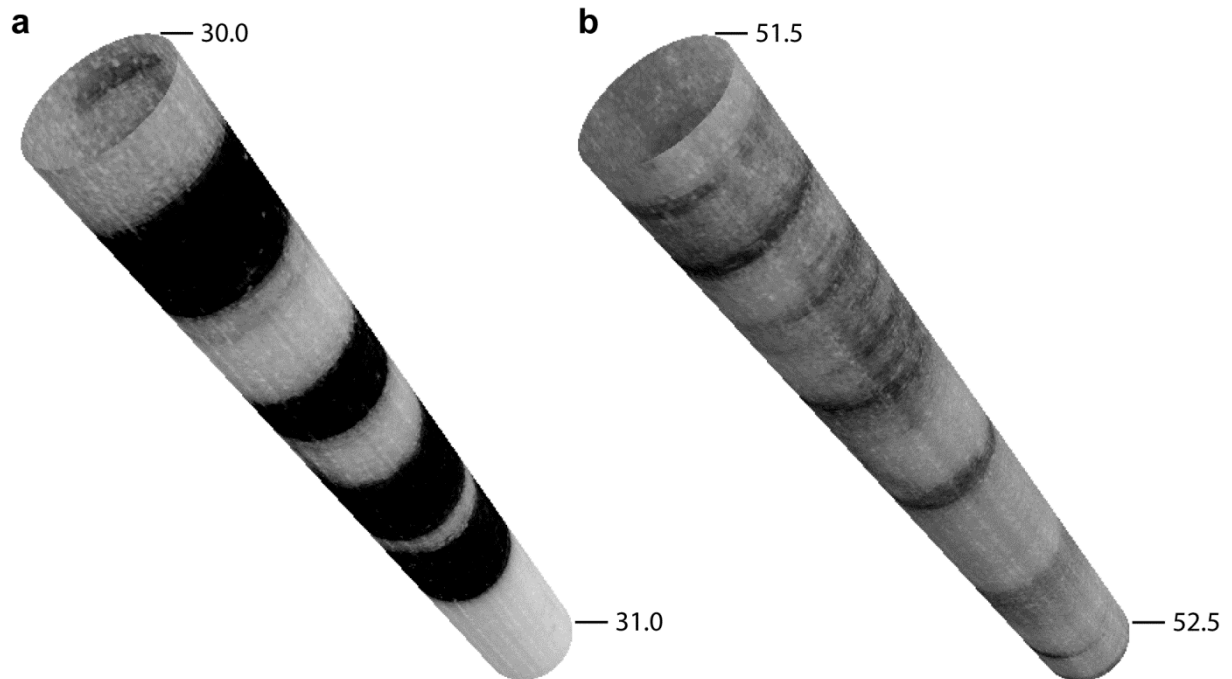
Figure 9: Expanded rolled OPTV images of two, 1 m-long virtual core segments from ice shelf core 10-S1 (Figure 8): (a) 30-31 m depth and (b) 51.5-52.5 m depth

The ice shelf cores, 08-S1 and 10-S1, both began in surface snow. However, while the former terminated in firn, the latter (being >66 m long) penetrated through the firn and into the underlying ice. Three specific characteristics of the OPTV images retrieved from 10-S1 were reported: (i) regular layering by dark bands, (ii) intermittent layering by thicker dark bands, and (iii) a general down-core decrease in luminosity. We interpret the first of these, the 'primary' layering, as annual layers similar to those previously identified on the basis of directional video by e.g., Hawley and others (2003) and Hawley and Morris (2006). In such logs, the darker zones mark the more melt-influenced icy layers formed during the summer and the lighter zones the colder winter accumulation. The summer layer spacing of ～1.0 m near the surface of 10-S1 accords with regional mass-balance approximations which indicate an accumulation of ～0.3 m water equivalent per year (van de Berg and others, 2006). However, this primary layering was frequently disrupted by the second layer type, which was darker (indicating less reflected light, consistent with bubble-poor ice) and had sharper boundaries with the matrix material. These characteristics, along with the intermittent occurrence of this 'secondary' layering along the borehole, are consistent with an interpretation as refrozen surface melt layers. Although comparison with the spacing of annual layers (below) suggests that these melt events do not occur each summer, they do appear throughout the full borehole length. The presence of these secondary melt layers also makes deriving an age-depth relationship for 10-S1 by primary-layer counting difficult. However, the age range of this borehole may be approximated by interpolating primary layer spacing from zones that are devoid of melt layers (e.g. 5-9 m, 17-19 m, 22-25 m, 36-40 m, 50-51 m and 56-60 m on Figure 8), suggesting that the record extends back for ～150 years from present. Although the frequent melt layers disrupt the core's potential to provide an undisturbed palaeoenvironmental record, they do provide independent

information on the scale and timing of major surface melting events, and directly affect only a minor proportion of the core's total length. Palaeoenvironmental reconstructions should therefore still be possible from cores such as this - as long as the physical influence of melting events is isolated and removed from the analysis. Finally, we interpret the general down-hole decrease in the luminosity of the OPTV image of 10-S1 (at a rate of 3.5 units per metre depth, averaged linearly over the full 66 m borehole length; Figure 8) in terms of progressive firnification, specifically the gradual isolation and coalescence of bubbles resulting in a net increase in the optical transmissivity (and concomitant decrease in reflectivity) of the borehole wall.

OPTV as a proxy for density profiles in ice shelves

The high sensitivity of the OPTV brilliance to the various ice type described above (melt layers, annual layers, large scale drift with depth) suggests there might a tight relationship to ice density, since the latter involves drastic changes in bubbles geometry and grain size that should both impact the optical response. This is what has been tested on representative cores from the 66.40 meters deep 10-S1 location. Figure 10 (left) summarizes density measurements obtained using either precise Mass/Volume determination on 2.5 cm cubic samples (M/V, black crosses), or high resolution RX tomography (Alfred Wegener Institute, courtesy of J. Freitag) at a resolution of 0.015 cm. Measurements are perfectly coherent, given the resolution difference. Figure 10 (right)
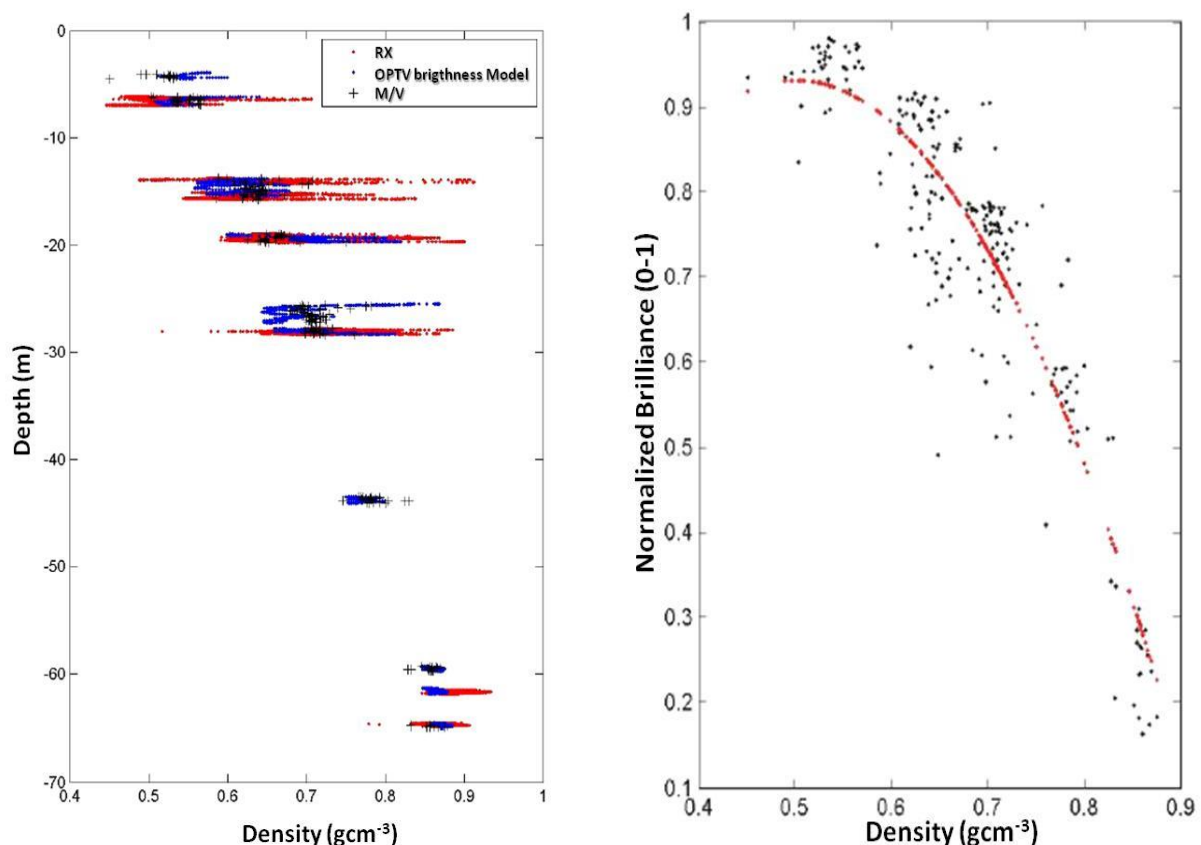

Figure 10: *Left*: Depth density profiles from Mass/Volume measurements (M/V), RX Tomography (RX) and calculated based on the empirical Brilliance-Density relationship (OPTV); *Right*: Normalized Brilliance/Density relationship for all individual M/V measurements. Sample resolution is 2.6 cm, 0.1 cm and 0.013 cm and for M/V, OPTV and RX respectively.

shows that we can indeed retrieve a polynomial empirical relationship (red dots) between the normalized OPTV brilliance (resolution 0.1 cm, mean of values at M/V resolution) and the density measured on the sample using the M/V method. A similar relationship can be obtained with the RX results. Applying this relationship in the selected cores gives the red dots in the left panel of Figure 10.

This opens the potential for retrieving fast, non-destructive (OPTV measurements can indeed be performed in any drill hole, including hot water drilling) high-resolution density profiles (with detailed structural information) which are of crucial interest to e.g. the interpretation of remote sensing data sets.

Identifying components of the "ice mélange", including marine ice

We drilled ten boreholes into the base of the rift proper and one was drilled into the ramp formed in the rift tip (Figure 5; Table 1). Several of these boreholes intersected apparently fundamentally different material facies. The OPTV log of 08-T1, cored for 38 m into the rift tip, was of uniformly high luminosity, similar to the material forming the matrix between the dark layers in 10-S1 (above). Indeed, the OPTV log of 08-T1 contrasts with that of 10-S1 in that the former is characterized by (i) fewer dark layers, and (ii) no apparent systematic decrease in the intensity of the background reflected light with depth.

All of the remaining 10 boreholes were drilled directly into the base of the rift (Figure 5), intersecting a series of material facies which always appeared in the same order but which were not all present at every borehole. These facies are as follows:

Surface snow. Snow was present in the uppermost sections of most rift boreholes and was identified visually at the surface and as a very bright backscatter in OPTV logs. Where present, this layer extended only for a few metres below the surface.

Granular ice. This facies, defined by a distinctively granular structure, was relatively massive and appeared as highly uniform on OPTV logs. However, the facies did occasionally contain isolated bubble clusters, particularly at depth. The facies was present in most rift boreholes, but it generally decreased in representation westwards, away from the rift tip. The upper surface of the granular ice also commonly coincided with the level of the saline-water table (sea-level) within the rift, and the two were always observed to be in close proximity. This facies typically extended for some metres below sea-level.

Marine ice. Progressing down-borehole, granular ice gradually gave way to a less massive and more strongly layered ice facies that was very similar in character to the marine ice imaged on the Amery Ice Shelf (Craven and others, 2009, Craven and others, 2005). This facies was present in all rift boreholes, either on its own or beneath the granular facies (and never above it), and showed an increased prevalence further west (away from the rift tip) as the thickness of the granular ice diminished. Indeed, in some of the most westerly boreholes, for example 08-R3, the marine ice facies extended the full thickness of the rift, cropping out at its upper surface (Figure 11, left). Although this facies appeared to be homogeneous in OPTV images, containing no notable bubble-defined layering, it was characterized by a green hue, particularly under transmitted
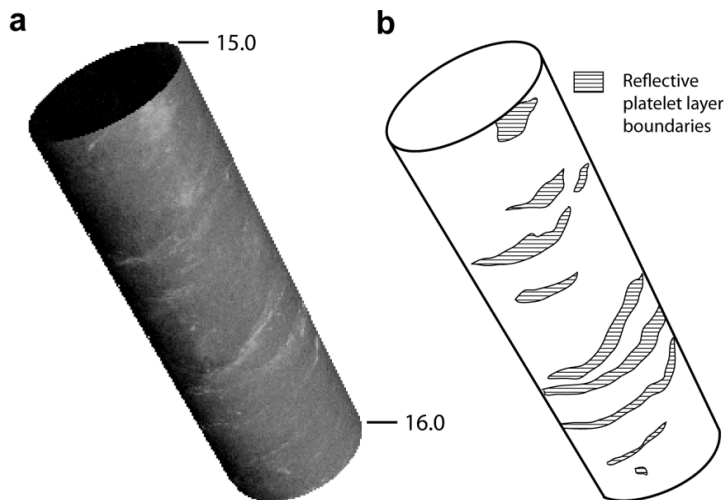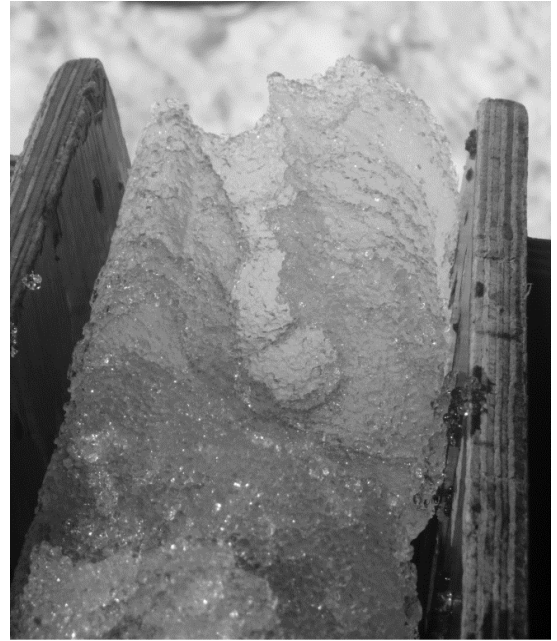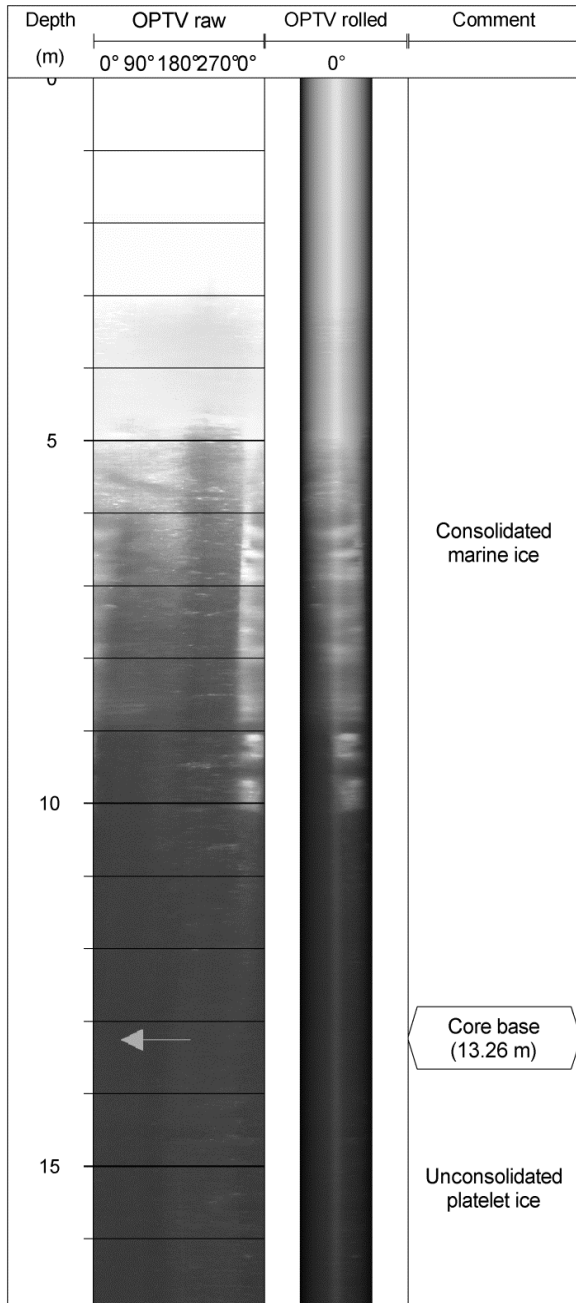
Figure 11: *Left*:. OPTV log of the full length of rift core 08-R3 with (progressing left to right) the raw OPTV image, the rolled OPTV image and annotations. No solid core was retrieved from below a depth of 13.26 m, where unconsolidated platelet ice was encountered. *Right top:* worm-like tubular conduit within core 10-R3. *Right bottom:* highly flaky, poorly consolidated marine ice aggregate. Bottom: Rolled virtual core image of a 1 m interval (15-16 m) near the base of core 08-R3 - a) OPTV image, b) interpretative sketch - brighter light areas are thought to represent boundary of layers of aggregated sub-ic-shelf platelets.

light near the surface. We interpreted this as due to the presence of a low concentration of chlorophyll-bearing marine algae, supported by occasional observations of dense patches of algae in core sections recovered from this facies. Such algae were not observed within the overlying granular ice. Although not clearly imaged by OPTV, core sections of marine ice did reveal the development of a strong sub-horizontal crystal alignment with depth, giving the facies a fissile texture.

One further notable aspect of this facies is that it contained sinuous tubular channels, similar in appearance to large worm holes (Figure 11 right top). These tubes were intersected by our cores on several occasions (e.g., 10-R3) and are typically 1-3 cm in diameter and appear to have no preferential orientation. Unfortunately, no OPTV log was recovered from a borehole segment intersecting such a tube, principally because most of the rift holes became blocked with buoyant ice platelets before OPTV logging was possible. However, the tubes were observed directly in the recovered core sections (Figure 11 right top).

Ice platelets. Towards the base of the rift cores, the marine ice became so fragile that it formed only a weakly-consolidated mass of thin platy crystals (Figure 11 right bottom). Below this point, the crystals were effectively unconsolidated and samples could no longer be retrieved by traditional coring (since the retaining core dogs could no longer hold the unconsolidated slurry within the barrel), effectively forming a seawater-saturated 'mushy layer' (Feltham and others, 2006). This transition marked the indistinct interface between the base of the solid ice shelf and the platelet-rich uppermost layers of the underlying seawater. One OPTV log, recovered from 08-R3 (Figure 10 left and bottom), did extend for ~4 m below the point at which solid core was no longer retrievable, thereby presumably penetrating the uppermost layers of the platelet-rich cavity. This lowermost section of 08-R3's OPTV log revealed the presence of unconsolidated material that was characterized by small-scale, sub-horizontal wavy layering (Figure 11 bottom), strikingly similar in appearance to that imaged by directional video at the base of the Amery Ice Shelf (figure 13 in Craven and others, 2005). These layers were repeated every few centimetres throughout the facies. Unfortunately, OPTV images could not be obtained from deeper into this facies because the buoyancy of the unconsolidated mass prevented further OPTV probe penetration.

Although providing clear contrasts between different ice facies, OPTV measurements adequately benefit from multiparametric measurements in the ice cores themselves.

$\delta^{18}O$ values for marine ice are close to $+2‰$, proving that it originated from freezing sea water (Gow and Epstein, 1972; Morgan, 1972; Oerter et al., 1992). Bulk salinity of consolidated marine ice at depth varies between 0.03 and 0.3 psu, which is two or three orders of magnitude higher than meteoric ice and one or two orders of magnitude lower than sea ice (Souchez et al., 1991; Tison et al., 1993; Khazendar et al., 2001; Tison and Khazendar, 2001).

Figure 12 summarizes basic physico-chemical properties (texture, T°, bulk salinity, $\delta^{18}O$) of the cores retrieved in 2008-2009. It is complemented by the data extracted from the 2010-2011 field season (Figure 13), note that the latter still await for the stable isotopes profiles (ongoing work).

Firn and meteoric ice in the region have negative $\delta^{18}O$ values (mean = -21.5 $\pm$ 2.2‰), negligible (below detection limits) salinity, and a polygonal granular texture. When soaked with sea water (as seen in the lower section of Core 08-R1 [B], Figure 12), the ice temperature increases to the freezing point of sea water (-1.9°C), causing crystals to become more rounded. Bulk salinity also increases (typically to 0.3-2 psu) in this facies, as does $\delta^{18}O$, indicating mixing between meteoric ice and frozen sea water.

The contribution from firn to the "ice mélange" appears to decreases westward within the rift zone. Core 08-R2 [D] shows a transition below ～5m with a sharp increase in $\delta^{18}O$ (becoming less negative), and slowly increasing salinities, down to 8-9 m depth (Figure 12). This transition zone could be caused by recrystallized soaked firn, or by snow ice (top layer of sea ice formed by flooding of the snow). The lower 10 m section shows a granular texture with constant positive $\delta^{18}O$ values and salinities ranging from 1 to 9, which is more typical of sea ice rather than marine ice. It is however highly unlikely that granular frazil sea ice (typically formed under conditions of turbulent winds) could accumulate to a total thickness of nearly 10 m. Under a turbulent regime, granular sea ice is quickly formed but can never attain depths of several meters, as the
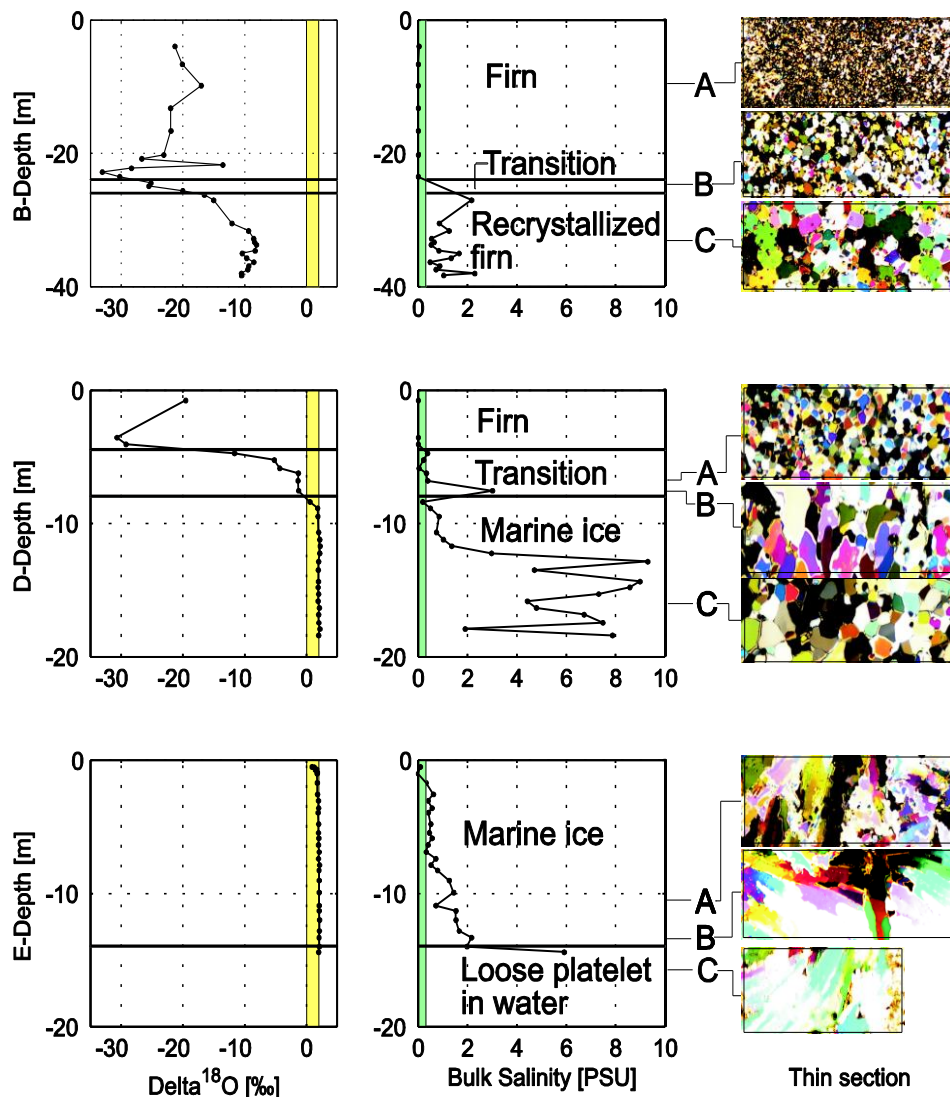
Figure 12: Isotopic composition, bulk salinity and texture for Cores 08-R1 [B], 08-R2 [D], and 08-R3 [E] drilled in the rift. The yellow and green bands show the reported ranges of $\delta^{18}O$ and bulk salinity for marine ice, i.e., 0-2‰ and 0.03-0.3 psu, respectively. Long axis side of thin sections is 4.5 cm. See Figure 2 and 5 for location of the drill sites.

turbulence has no effect anymore once the sea ice cover is sufficiently thick. In that case, columnar sea ice is more likely to form (Martin, 1981). We therefore favour a marine ice origin, for the lower section of the core, with recent consolidation in near-surface conditions explaining the higher salinity (Tison et al., 1998).

Figure 13: Basic physic-chemical properties of the 2010-2011 rift ice cores (ongoing work)

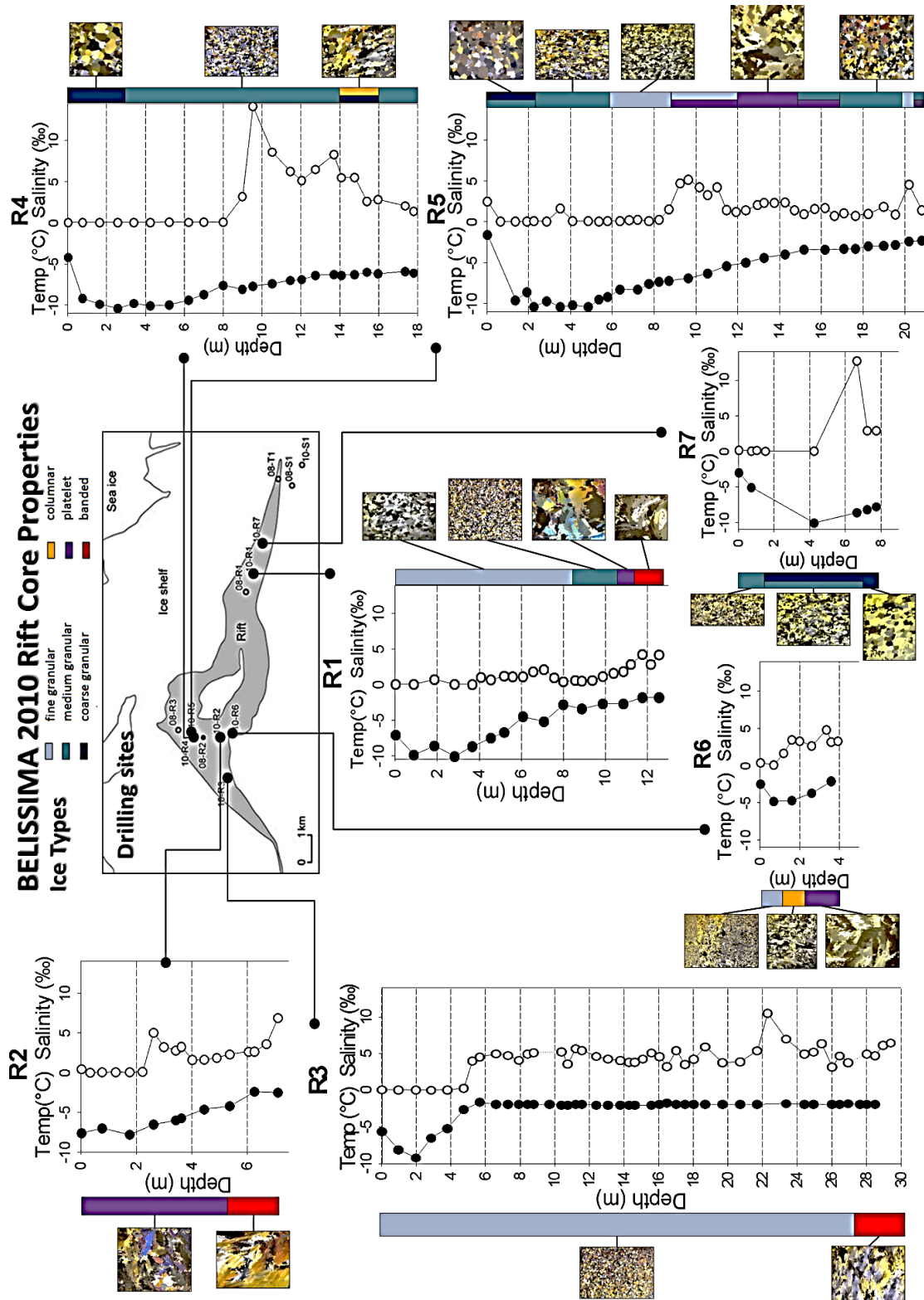Core 08-R3 [E] (Figure 12) is characterized by the absence of any snow/firn and shows ~12 m of marine ice outcropping at the surface in association with a dense network of crevasse fills. It also shows a regular increase of the salinity in the lower, younger layers. Here, the last 10 meters (at least) of marine ice show a characteristic "banded" facies inherited from the constitutive platelets. In contrast, the marine ice in core 08-R2 [D] (Figure 12) is only granular suggesting a different genetic process. This configuration is indeed similar to that described by Tison et al. (1998) at the front of Hells Gate Ice Shelf, Antarctica, where the strong contrast in marine ice texture (granular as opposed to banded) was attributed to water circulation below the shelf.

The new set of 2010-2011 cores in Figure 13 confirms the dominance of firn ice in the ice mélange, at both ends of the rift (see e.g. 10-R3). Banded marine ice is limited to the central part of the rift, and to its bottom few meters (red colour in Figure 13). Strangely enough, cores 10-R4 and 10-R5, located in the vicinity of core 08-R3 [E] predominantly show granular ice. Here, ongoing $\delta^{18}O$ measurements are needed to confirm if we are in presence of marine ice. This area of the rift, close to an internal iceberg, is quite heterogeneous and hilly, showing clear traces of crevasses fillings within a potentially different matrix.

With these ice cores properties in mind, we can return to the interpretation of the various OPTV facies observed in the rift. The material imaged in the rift tip (08-T1) was similar to that forming the matrix of 10-S1. However, in contrast to the OPTV log of 10-S1, that of 08-T1 is uniform and includes only three slightly darker layers that are each only a few centimetres thick. Further, luminosity does not decrease measurably with depth along 08-T1. We interpret these properties, in association with the location of the borehole in the rift tip, as indicative of infilling by blown snow (as opposed to surface firnification on the ice shelf; above). This process, described by Leonard and others (2008) for a rift on the Ross Ice Shelf, would result in little or no seasonal signal, while the possible rapidity of aeolian in-filling may also explain the absence of firnification-related bubble nucleation with depth.

Within the rift proper, we interpret the uppermost granular ice facies as snow and firn that have become saturated by percolating saline water, causing the observed grain rounding. This interpretation is also consistent with the general thinning of this facies westwards, away from the apex of the rift, where the rate of surface accumulation by snow trapping is expected to be lower. As described above, progressing westwards and with depth into the base of the rift, this facies gives way to the marine ice facies. All of the properties of this facies, and in particular its occasional high algal content and gradual disintegration into unconsolidated platelets at the base of the rift boreholes, suggest formation by the progressive accumulation and compaction of buoyant platelets formed within the sub-ice-shelf cavity, consistent with previous interpretations. The fact that these platelets rose up the water column rapidly in completed boreholes, commonly preventing OPTV access within some minutes of drilling penetrating the cavity (08-R3 being the sole exception in this study), indicates that the platelets were both buoyant and mobile. The ubiquitous presence of this facies within our rift boreholes, typically to a thickness of some metres to tens of metres, also indicates that platelet marine ice formed throughout the rift.

Finally, the unique observations of worm-hole-like tubes within the granular ice and marine ice facies provides clear evidence of conduit-based water flow through the lowermost layers of the rift mélange. We assume that these conduits are formed during the early stages of ice formation, when the material is still erodible, and then become frozen-in as the material consolidates and (possibly) dewaters. It is therefore apparent that this marine ice is highly porous and permeable, consistent with previous indications (e.g., Craven and others, 2005). One characteristic of marine ice that remains poorly understood is its very low measured bulk salinity (typically in the range 0.05-0.5 ‰; e.g., see summary in Tison and others, 2001) relative to that measured in sea ice (typically in the range 1-20 ‰; Weeks, 2010), despite both ice types being formed by the aggregation and consolidation of frazil ice frozen from seawater. Eicken and others (1994) argued that the standard mechanisms of post-formational desalination proposed for sea ice are in fact insufficiently effective to reduce the salinity of marine ice to measured values. Instead, these authors tentatively invoked a mechanism of saltwater expulsion from already low-salinity platelets during buoyancy-driven aggregation and densification. Tabraham (1998) introduced the 'mushy layer' concept into a solidification model for marine ice. In this approach, relatively recently proposed to describe the desalination process in sea ice, convective movements in the interstitial liquid are driven by density instabilities due to salinity gradients in a temperature field increasing downwards. It leads to the development of convective 'chimneys' known as 'brine channels' in sea ice, exporting salts from the mushy layer to the ocean below. However, Tabraham (1998) also recognised that, although the model of drainage through channels produced some desalination in marine ice, the amount of desalination was found to be less than the levels observed within actual marine ice, the main problem being shut-down of the flow with continuing solidification. The author suggested that combining mushy layer desalination with compaction might be sufficiently efficient to reach the observed low salinity values. Alternatively, Tison and others (2001) showed that, by treating marine ice is a two-phase compound (pure frazil ice crystals in a consolidating interstitial fluid) and applying a boundary layer model for the consolidation of the interstitial liquid, marine ice salinities could be reproduced if fractionation coefficients derived from the solidification of freshwater ice were used rather than those for columnar (dendritic skeletal layer) seawater ice.

The 0.05-0.5 ‰ salinity range discussed above has generally been observed in thick (10^2-10^3 m) marine ice layers and, to the best of our knowledge, no internal desalination chimneys (either active or relict) have (until now) been described in such layers. The marine ice salinity range in our RBIS data set covers a range more typical of sea ice ($\leq$ 9 ‰ in the lower layers), with very low salinities (0.1 ‰) only being measured in the upper few metres over a total thickness of a maximum of 10-20 m (Pattyn and others, in review). The occurrence of the worm-hole-like tubes in the less consolidated lower layers could therefore represent the signature of mushy-layer-like convection processes in the early stages of consolidation of the marine ice layer. The fact that these tubes lack the typical vertical tree-like structure of sea-ice brine channels might reflect the geometrical control of the sub-horizontal accumulation pattern of the loose large frazil ice platelets. An alternative (or additional) hypothesis is that, once the marine ice layer is formed, salt would continue to be expelled from the layer by freezing-front-rejection accompanying on-going recrystallization within the layer. The removal of that salt-rich water through an effective internal drainage system would then decrease the bulk

salinity of the remaining marine ice. Such a process would also involve the delivery of relatively high-salinity water to the underlying water column.

In principle, the thickness of a marine ice layer beneath an ice shelf that is in hydrostatic equilibrium could be determined by comparing the measured surface elevation of the floating shelf with the surface elevation calculated from buoyancy (Corr et al., 1995; Fricker et al., 2001). In practice, especially for moderate marine ice thickness (few 10's of meters), the calculation is hampered by large uncertainty in the density profile through the shelf, and uncertainties and ambiguities in the radar-detected ice thickness (see below).

Observations of modified CDW underneath RBIS

Bathymetric measurements in front of a fringing East Antarctic ice shelf in Dronning Maud Land (23-27°E), unofficially named Roi Baudouin Ice Shelf (Nishio et al., 1984) or 26°E ice shelf (Pritchard et al., 2012) along the Princess Ragnhild Coast (Figure 3) were carried out during the 1960s (Derwael, 1985) and the mid-1980s (Iwamani and Tohju, 1987; Iwanaga and Yohju, 1987). These data show a deep trough cutting into the continental shelf at 25.5°E, with a maximum depth of more than 700 m b.s.l., but data *sampling* remained outside the areas of significant pack ice. New observations by sonic depth ranging and physical oceanographic full-depth casts in December 2011 (black shading in Figure 14) demonstrate that the trough is more than 850m deep, with depths
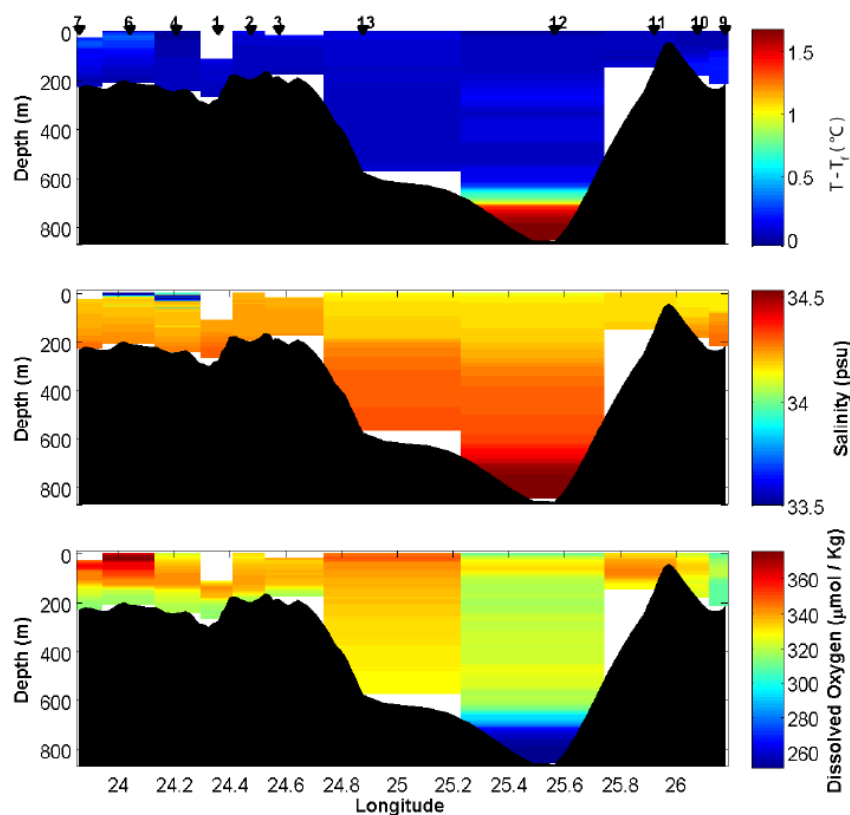
Figure 14: North-Facing Oceanographic Sections. Results of CTD measurements are plotted here such that column widths are proportional to the distance represented by individual casts. These casts were made along a roughly ice front parallel line following latitude 70°10'S (see Figure 3 - yellow dots connected by line). Bedrock topography is from bathymetric measurements (Derwael, 1985) and CTD casts. Water temperature relative to the local freezing point (top) was calculated following Holland and Jenkins (1999); salinity (middle) and dissolved oxygen (bottom). The three panels demonstrate the presence of warm, salty, low-oxygen water in the deepest part of the trough, characteristic of warm mCDW. (also see Figure 15).

greater than 800m (sonic ranger's limit) over a shelf-parallel distance of several km. This trough is located beneath the seaward extension of the central flowline of Western Ragnhild Glacier, the source of this ice shelf (Pattyn et al., 2005).

The presence of such deep troughs cut into the continental shelf is the most effective mechanism by which warm salty low-oxygen CDW can access the cavities beneath Antarctic ice shelves (Potter and Paren, 1985; Jacobs, 1991; Dowdeswell et al., 2006). CDW is denser than Antarctic coastal surface waters, and typically lies at greater depths close to the continental shelf than it does several kilometres away from the ice-shelf edge. To cross the continental shelf break and access the grounding line of the Antarctic ice sheet, CDW must exist at depths allowing access to the continental shelf. This could be achieved through atmospheric pressure gradients (Meredith et al., 2012), through mixing and eddy transport within the Antarctic Slope Front (ASF; Nøst et al., 2011), or via troughs cutting the continental shelf at greater depths than the local pycnocline (Jacobs, 1991), as is the case at 25.5°E.
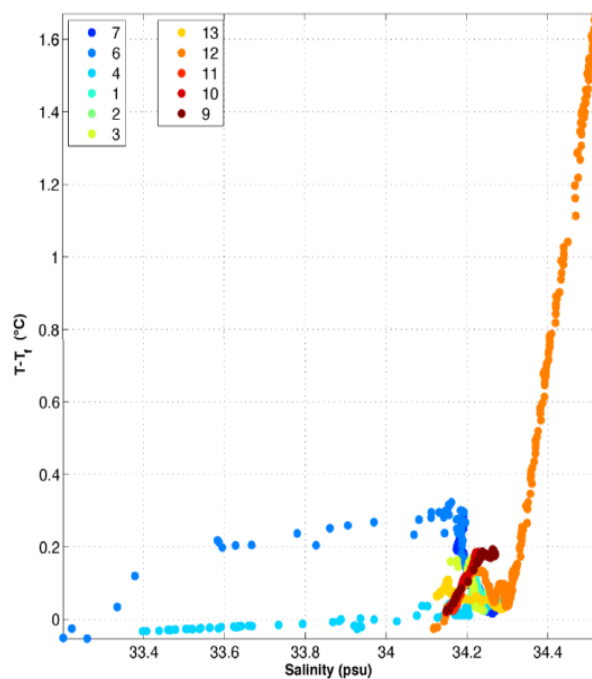

Figure 15: Temperature excess (measured temperature minus calculated freezing / melting temperature following Holland and Jenkins (1999)) versus salinity for the 11 casts displayed in Figure 14. Cast 12 clearly depicts mixing values typical of mCDW.

As mentioned above, high and accelerating rates of underwater erosion of ice shelves in the Amundsen and Bellingshausen Seas of West Antarctica are significantly impacting the mass balance of the Antarctic Ice Sheet, hence contributing to observed global sea level rise. This erosion takes place because circumpolar deep water with temperature and salinity well above those typical of Antarctic continental shelf waters comes into contact with the ice shelves (Jacobs et al., 2011; Jenkins et al., 2010). Along most of the Antarctic continental shelf break, the Antarctic Slope Front (ASF; Jacobs, 1991) forms a dynamic barrier to the intrusion of CDW onto the continental shelf. Mixing of CDW with continental shelf waters along this barrier results in "modified CDW" or more typically along the East Antarctic coastline "highly modified" CDW, with salinities and

temperatures that are slightly too high and dissolved oxygen content slightly too low to be explained by ice shelf interaction or continental shelf water properties, but far from the values expected for pure CDW.

A strong thermocline is observed at 650-700m depth within our 25.5° trough as shown in Figure 14. The warm salty oxygen-depleted water found between 700 and 850m, clearly results from mixing of cool fresh shelf waters with the CDW found offshore, as also shown in the TS diagram of Figure 15 (mCDW).

In a full-depth 1000m cast on the continental slope just north of this study's observations (Iwanaga and Yohju, 1987), warm salty CDW / mCDW was found between 500m and the bed (red oval in the flow line schematic of Figure 16). The maximum recorded temperature in that cast of 0.75°C at 600m depth is just less than 1°C warmer than the maximum temperature of -0.2°C measured below 700m on the continental shelf in 2011. Deep water salinities recorded in the same cast (Iwanaga and Yohju, 1987) are lower (∼34.687 PSU) than documented for CDW off the West Antarctic coastline, suggesting that the relatively low dilution of the CDW temperature signal may be due to a locally weak ASF resulting from a low gradient in salinity between the shelf and offshore waters (Jacobs, 1991). An analogous continental slope temperature measurement offshore from the Shirase Glacier (at 38.5°E) was used to infer an ocean temperature excess of 2.9°C at its grounding line (Rignot and Jacobs, 2002), assuming zero dilution of the temperature signal across the ASF.
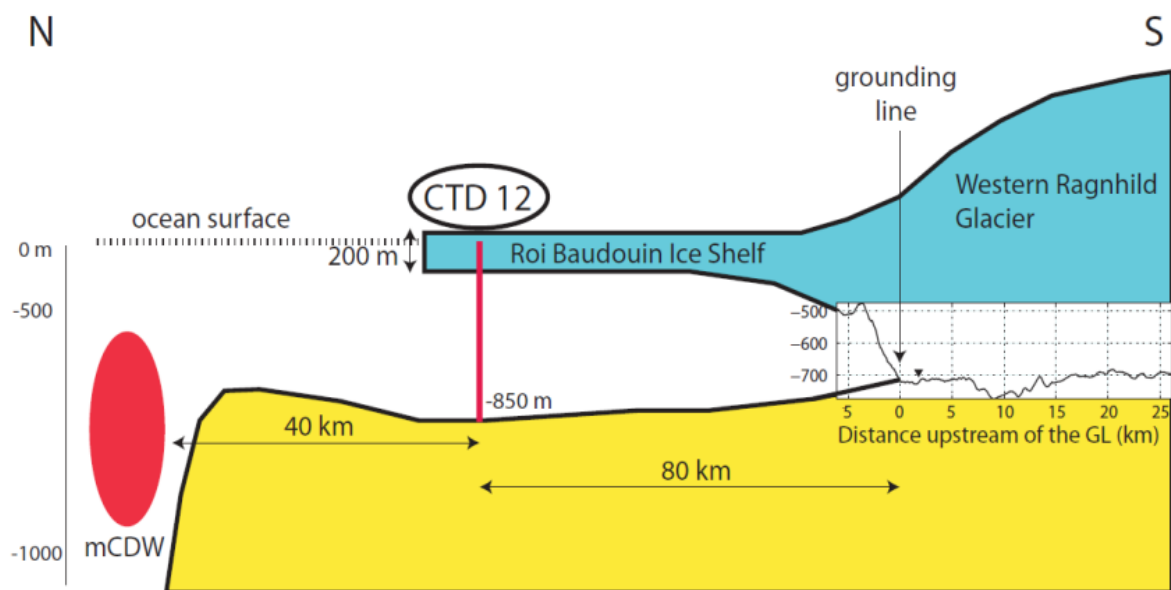
Figure 16: Flowline schematic of the Western Ragnhild Glacier. This cross section of the ice shelf-ice sheet-ocean setting of the Western Ragnhild Glacier follows the dashed line in Figure 3. Warm mCDW was found at CTD-12 on the continental shelf underneath the ice shelf and was previously observed on the continental slope and deeper ocean (red oval, Iwanami and Tohju, 1987,Iwanaga and Yohju, 1987). All vertical positions are relative to local sea level (geoid correction), with significant vertical axis exaggeration. The inset figure (white rectangle) shows a detail of the sub-shelf and sub sheet topography obtained from the radar data and plotted here with respect to the WGS84 datum including the position of the grounding line.

The continental shelf waters in our study area are cool and fresh (Figure 14), with extensive platelet ice formation, indicative of interaction with upwelling ice shelf water (Gough et al., 2012). The cool fresh shelf water also has relatively high dissolved oxygen concentrations (Figure 14), suggesting that it is largely derived from winter surface waters and the early-summer melting of sea ice. This contrasts with the dramatically lower oxygen concentrations of the warm salty mCDW layer, demonstrating its lack of recent exposure to the atmosphere.

The in-situ freezing temperature of seawater is strongly influenced by salinity. The difference between measured temperatures and the in-situ freezing temperature calculated following (Holland and Jenkins, 1999) is plotted in Figure 14. mCDW found between 700 and 850 m depth in the trough is 1.7°C warmer than the in-situ melting temperature of ice (Figures 14 and 15). Several parameterizations exist for determining the basal melt rate of an ice shelf as a function of the temperature difference between observations and the local freezing temperature. Following Rignot and Jacobs (2002), the water below 700m in this trough is capable of melting around 20m per year at an ice sheet grounding line, provided it comes into contact with it.

The grounding line of the outlet glacier feeding this ice shelf is 80km to the south of the oceanographic cast in the trough, and the ice goes afloat from roughly 750m depth (Figures 16 and 17). Given the depth at which the mCDW layer is found and inferring a relatively smooth trough shape, the observed mCDW should easily exist at the same depth as the grounding line (Figure 16). The measured radar profile just downstream of
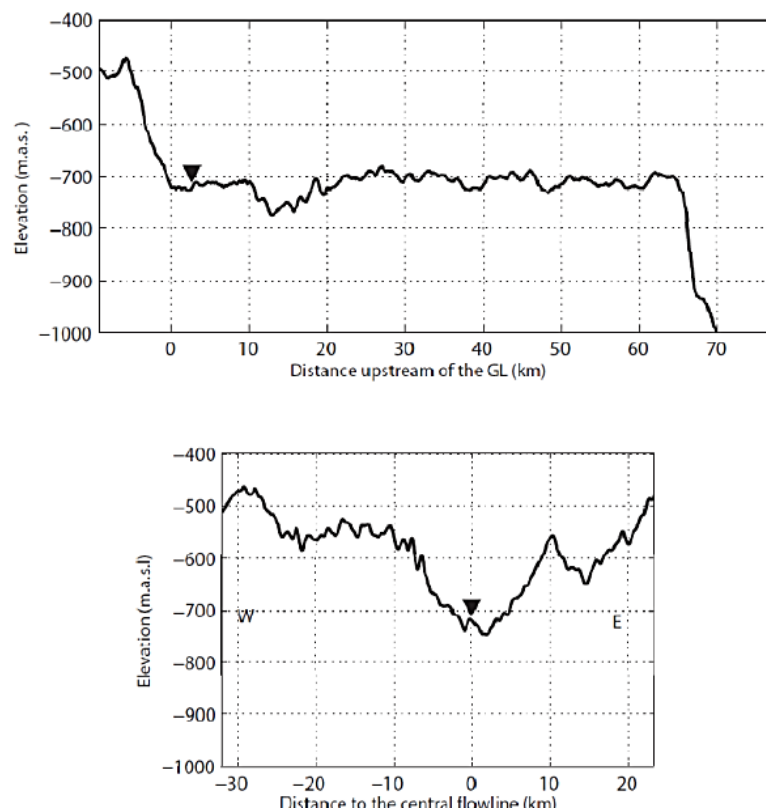
Figure 17: Longitudinal profile of bedrock elevation and sub-shelf topography (top panel) and cross-sectional bedrock topography at the grounding line (lower panel). The inverted triangle in both panels shows the intersection of both profiles. The deepest part of the profile at the grounding line is 750m b.s.l. (bottom panel), which is at the same depth of warm mCDW found in cast 12, 80 km downstream from the grounding line. The relatively flat area upstream of the grounding line stretches at least 60km inland (top panel).

the grounding line shows that the ice shelf thins by 200 m within 5km downstream after going afloat. This thinning is not easily explained by dynamics as there is a lack of convergence in the ice flow in this region, and is thus supportive of melting near the grounding line.

Resolving the "conundrum" of Marine ice rheology

Because it mainly accretes in "weak" locations, marine ice plays a crucial role in ice shelf stability. Little is known however on the rheology of this particular material (low salinity, no bubbles, and specific fabrics). Using inverse modelling, Khazendar et al. (2009) has concluded that potential locations of marine ice accretion show lower inferred viscosities, suggesting *marine ice deforms faster than meteoric ice*. However, in preliminary experimental compression tests, Samyn et al. (2007) and Dierckx et al. (2010) provide *evidence of the opposite*.

We therefore investigated the rheological properties of marine ice samples originating from the Nansen Ice Shelf (Ross Sea, Antarctica - Khazendar et al., 2001; Tison and Khazendar, 2001), across the [-10°C to -3°C] temperature range under vertical compression in unconfined conditions and compare them with both results from artificial and natural isotropic ice (referred here as clean ice) deformation in a similar stress setting (Jacka, 1984; Budd and Jacka, 1989; Jacka and Li, 1994) and predictions from the empirical relationship proposed by Paterson (1994) and recently updated by Cuffey and Paterson (2010).

Because of its crucial importance in ice dynamics modelling, much attention has been given to the value of the creep parameter A in Glen's flow law for ice deformation (Eq. 10, Glen, 1958).

$$\dot{\varepsilon} = \left| A \sigma^n \right.$$

10

In their recent synthesis of prior research (for example Budd and Jacka, 1989), Cuffey and Paterson (2010) concluded that for practical applications the parameter A should be dissociated into an effect of the temperature field (Arrhenius law) and effects of intrinsic material properties such as grain size, c-axis orientation fabric, impurities and water content. Their relationship is Eq.(11),

$$\dot{\varepsilon}_{jk} = A E_* \tau_E^{n-1} \sigma'_{jk}$$

$$A = A_* exp\left(-\frac{Q_c}{R}\left[\frac{1}{T_h} - \frac{1}{T_*}\right]\right)$$

$$with \quad \tau_E^2 = \tfrac{1}{2}\Sigma_{j,k}\left(\sigma'_{jk}\right)^2$$

$$and \quad \sigma'_{jj} = \sigma_{jj} - \frac{1}{3}\left(\sigma_{ii} + \sigma_{jj} + \sigma_{kk}\right)$$

11

in which: ϵ is the deformation rate, A the creep parameter, E_* the enhancement factor that takes into account the combined effect of all intrinsic factors, τ_E the effective shear stress, σ' the deviatoric stress (the crossed terms are zero on uniaxial compression), σ the normal stress component, A_* the constant prefactor (the value of A at the reference temperature $T_* = -10°C$, Q_c [J mol^{-1}] the activation energy for creep, R the universal gas constant and T_h the pressure dependent temperature in Kelvin (Hooke, 1998; Schulson and Duval, 2009; Cuffey and Paterson, 2010). The octahedral shear stress that will be used in this paper, is defined by $2\tau^2_E = 3\tau^2_{oct}$. Considering ice shelf meteoric ice as the best equivalent of typical isotropic meteoric ice ($E_* = 1$), these authors use its observed/modelled mean A value at -10°C (A= 3.5 10^{-25}s^{-1}Pa^{-3}) as the reference value for A_* (with n=3). While field and experimental measurements agree on a value of $Q_c = 60$ kJmol^{-1} for the activation energy if $T_h < T_*$, they select $Q_c = 115$ kJmol^{-1} for the temperature range [-10°C to 0°C] Weertman (1983), in order to match the results of inverse modelling of the flow of temperate glaciers. The authors (Cuffey and Paterson, 2010) then recommend different values for the enhancement factor, ranging from 1 to 5, depending of the grain size, impurity content, fabric, etc. Equation 11 presents the advantage of separating the temperature and material dependent parameters A and E_*, respectively.

The Nansen Ice Shelf (NIS) is located in Terra Nova Bay, Victoria Land, East Antarctica (Khazendar, 2000, Khazendar et al., 2001; Tison and Khazendar, 2001). Here marine ice forms in rifts opening throughout the entire ice shelf thickness (few hundred meters) at the grounding line and downstream, outcrops at the ice shelf surface, due to net ablation from severe katabatic wind regimes. Two 45 m ice cores have been collected during the 1995-1996 austral summer in the framework of a Belgo-Italian drilling program. The two ice cores were located along a central flow line of the ice shelf at respectively 7.5 km (NIS1 – 74°51'S 162°50'E) and 24.5 km (NIS2 – 75°00'S 163°06'E) downstream from the grounding line. All cores had a diameter of 8cm and were collected with an electro-mechanical (SIPRE-type) ice corer.

A selection of 10 marine ice samples has been chosen from the NIS1 and NIS2 marine ice cores. Samples were shaped as cylinder of +/- 3.5 cm diameter and +/- 7 cm tall. Physical properties along the length of the cores were examined with thin sections following the conventional procedure of Langway (1958) and analyzed for texture and fabric using a G50 LED-White Automated Fabric Analyzer (Russell-Head and Wilson, 2001; Wilson et al., 2003). The salinity of each sample was deduced from Cl$^-$ anion determination, using HPLC (Dionex ~ 100) measurements (precision < 4%). Assuming that the Cl$^-$ salinity ratio does not change during formation or melting, bulk ice salinity is deduced from the mean Cl$^-$ salinity ratio in sea water (19.35/35) (Sarmiento and Gruber, 2006). Although this is clearly an approximation with limited accuracy (0.03 +/- 0.0012 to 0.3 +/- 0.012), we consider it as sufficient for the purpose of this study.

We aimed to select samples with ice fabrics as close as possible to a random crystal orientation distribution. The salinity range usually encountered in marine ice (0.03 to 0.3 - e.g. Tison et al., 1993; Tison and Khazendar, 2001) allows us to test the contribution of the salinity to the enhancement factor E_*. Finding marine ice with an isotropic fabric was a significant challenge, given the specific setting of the NIS marine ice outcrops, prone to develop sustained folding [see Khazendar et al., 2001]. Figure 18

shows two examples of textures and fabrics from the NIS1 core. Most of the selected samples showed crystallographic properties similar to sample NIS1-59c, i.e. a fabric reasonably close to random. A few samples had however to be selected in more oriented ice (eigen vector S1 close to 0.77, Figure 18), such as sample NIS1-82b, with sub-vertical folds and crystal elongation. Samples of low (min. 0.027) and high (max. 0.234) bulk salinities were chosen for each of the selected temperatures, as shown in Table 2. The experimental temperatures were designed to adequately cover the usual range of observed temperatures within ice shelves (e.g. Zotikov, 1986). The grain size was homogeneous between samples, with a mean value of 1.65 mm².

The samples were deformed in unconfined uniaxial compression using the pneumatic device developed at the Laboratoire de Glaciologie of the Université Libre de Bruxelles and described in details by Samyn et al. 2011.

NIS1 – 59c

S1 = 0.5867
S2 = 0.2866
S3 = 0.1267
n = 622 points   (quality 75%)

1068 points

NIS1 – 82b

S1 = 0.7673
S2 = 0.128
S3 = 0.1047
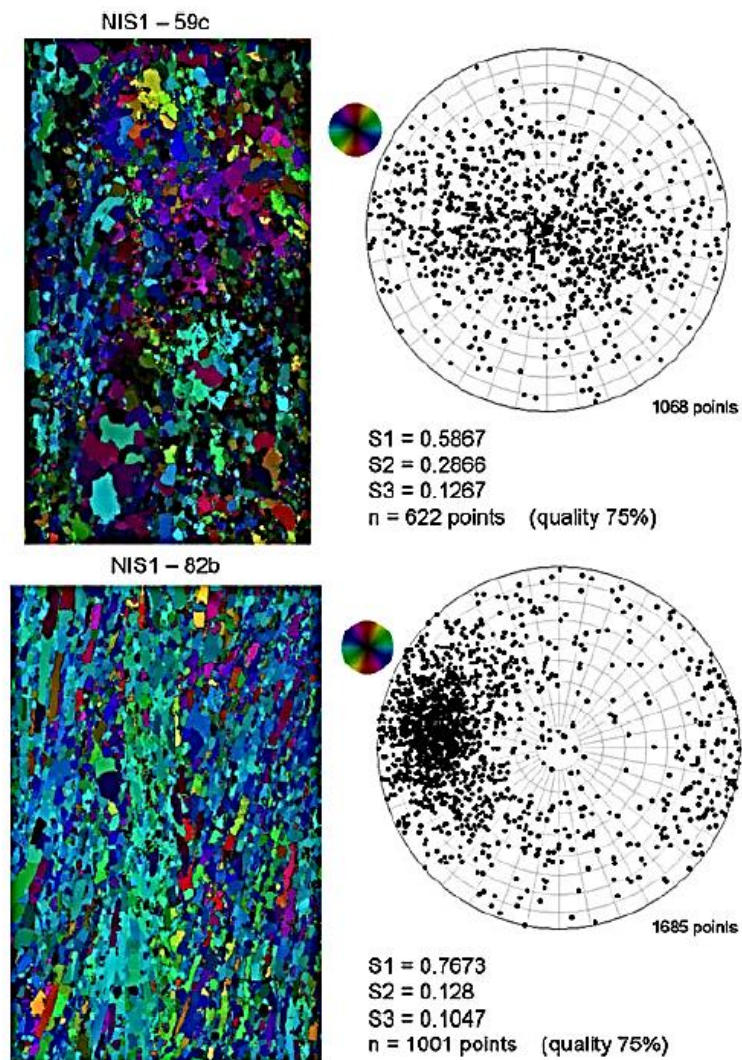n = 1001 points   (quality 75%)

1685 points

Figure 18: Typical sample fabrics before compression experiment, using an automated fabric analyser system (G50). Thin sections are vertical and shown with artificial color corresponding to c-axes orientation. Sample NIS1-59c is representative of most of the marine ice samples used. A few samples show a more oriented fabric, as represented by NIS1-82b.

Sample ID	Experimental Temperature [°C]	Salinity [—]	Mean Grain Size [mm^2]
NIS2 53c	−3	0.234	2
NIS1 82b	−3	0.047	1.45
NIS2 96a	−3	0.055	1.9
NIS1 97d	−6	0.035	1.45
NIS1 74e	−6	0.051	1.4
NIS1 59c	−6	0.089	1.85
NIS1 91b	−6	0.057	1.5
NIS1 49b	−10	0.131	—
NIS2 53b	−10	0.224	2
NIS2 4a	−10	0.027	1.35

Table 2: Temperature, salinity and grain size of the marine ice samples used in the deformation experiments.

As in previous studies, the aim of the deformation experiment is to reach the secondary creep at which the strain rate is minimal. Minimum creep is a unique point within the ice creep curve that allows for comparison between the effects of the properties of one ice type as compared to another. Each sample is submitted stepwise to an increasing stress, beginning with a stress close to 0.1 MPa and incrementing up to a maximum of 0.8 MPa. This procedure allows to keep the same sample for different applied stresses, and therefore keep the same parameter 'A' to analyze only the parameter 'n'. At each step, the secondary creep stage is achieved, with its recorded associated minimum strain rate. It should be noted again that using secondary instead of tertiary creep means that pre-oriented fabric can play a role on the viscosity, resulting in dispersion in the data set. Combining these stepwise records in a log-log plot then allows easy representation of Glen's flow law and deducing values for the "n" and "A" parameters. We also compared the stepwise load approach with a continuous case to check for the validity of the former. For this, sample NIS1-91b has been directly loaded to 0.67 MPa. The obtained data point perfectly fits with the determined trend.

Figure 19 summarizes the results of our compression deformation tests at the three selected temperatures (red triangles). Each symbol is an experimental data point which represents the minimal strain rate at secondary creep for a given applied stress (octahedral shear stresses and strain rates are used here to ease the comparison with the other data sets (Schulson and Duval, 2009). The red lines are linear fits through each of these experimental data sets. Also shown in Figure 19 are a) previous experimental results obtained in uniaxial compression on clean ice (blue symbols- Jacka, 1984; Budd and Jacka, 1989; Jacka and Li, 1994)) and b) empirical laws from Paterson (1994 - black dashed line) and Cuffey and Paterson (2010) for $E_* = 1$ (black solid line).

The mean slope of the linear fits through our data sets is 2.93 +/- 0.11, while the equivalent value for clean ice (all temperatures, through all data - Jacka, 1984; Budd and Jacka, 1989; Jacka and Li, 1994) is 3.29 +/- 0.2, but closer to n = 3 for each data set considered separately. This further supports the choice of n = 3 in Glen's flow law, for octahedral stresses ranging between 0.1 and 0.8 MPa.

The variability around each marine ice trend can be explained by the crystal orientation fabric variability of the different samples. Indeed, it can be expected that some samples

are harder or softer in compression compared to more isotropic samples. These effects will be discussed in detail in the future (in preparation).
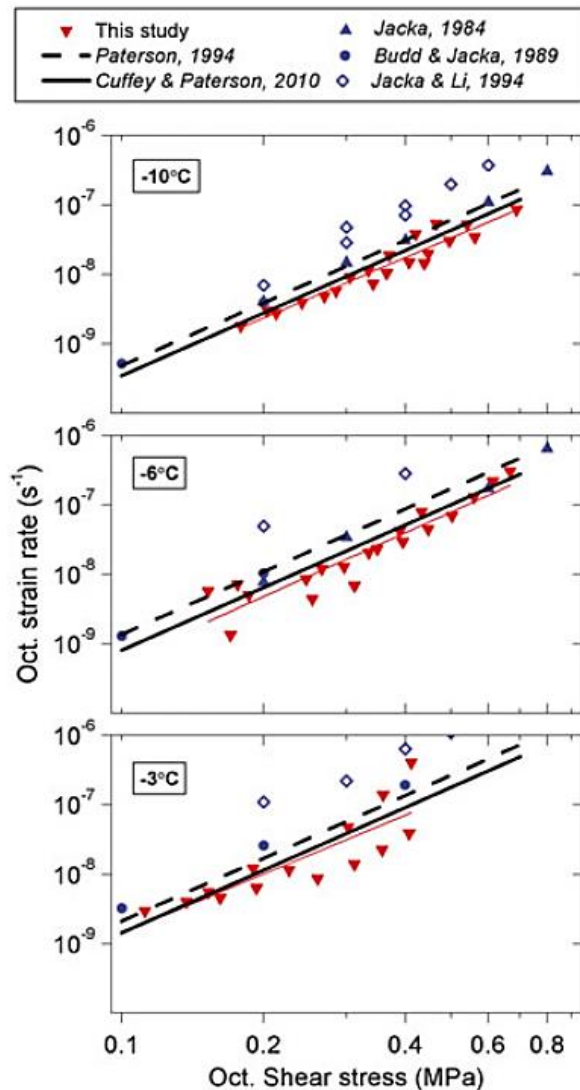

Figure 19: Comparison between this study (marine compression experiments, in red), clean ice compression experiments (artificial and natural isotropic ice), Jacka's data, in blue and literature (Paterson and Cuffey experimental laws, respectively, in dashed and solid black line). The mean slope of all our linear fits is around 2.93 ± 0.11. marine ice data match the new calibration established by Cuffey and Paterson (2010).

Clear differences however exist between the various data sets in Figure 19 in terms of the relative position of each trend. These differences represent the relative "softness" of the ice, as would be expressed in the enhancement factor E_* of the creep parameter A, following the approach of Cuffey and Paterson (2010). As underlined in preliminary results from Samyn et al., 2007 and Dierckx et a;. (2010), it appears that at all temperatures, marine ice samples are harder to deform than clean ice. This is therefore also the case, when compared to the relationship proposed by Paterson (1994), drawing considerably from the results of these experiments. However, the linear fits of our datasets are close to the trends of Cuffey and Paterson's empirical law, calculated for the lower boundary case of an enhancement factor $E_* = 1$, and this throughout the whole temperature range (i.e. using the appropriate values of the activation energy, depending on the temperature range). It therefore appears that marine ice recently consolidated into ice shelves provides an excellent natural example of isotropic ice with minimal viscosity. Our new data set also offers experimental validation of the lower boundary of

Cuffey and Paterson (2010) relationship throughout the temperature range, for stresses greater than 0.1 MPa. It follows that isotropic marine ice does not deform specifically harder than other ice types but rather represents the lower boundary for natural ice deformation, with an enhancement factor equal to 1.

As discussed above, none of the chosen samples has a truly isotropic c-axes distribution, which might explain part of the spread of our data points around Cuffey and Paterson's relationship in Figure 19. These excursions are worth considering further in terms of potential other drivers. A wide range of solid and soluble impurity contents has been described in the marine or meteoric ice literature (e.g. Jones and Glen, 1969; Oerter et al., 1992; Tison et al., 1993; Moore et al., 1994; Trickett et al., 2000; Khazendar et al., 2001; Treverrow et al., 2010) and these can also potentially affect the E_* value. Even though our samples covered a relatively large salinity range, no significant systematic deviation could be isolated in the studied range of temperature and stresses. It therefore seems likely that the soluble impurity content plays a negligible role in the enhancement factor for the whole documented range of marine ice samples. Differences in the concentration or granulometry of the solid impurity content could also be responsible for some deviations in our data set, but this factor could not be quantified in the present study. The ice grain size is shown to be homogeneous within our samples set and cannot therefore be held responsible for the dispersion of the data. Finally, the higher spread is observed at -3°C, indicating a much higher sensitivity to sample and/or experimental conditions at warmer temperatures.

It is, also important to underline that our experimental data set covers the range of 0.1 to 0.8 MPa for applied stresses. This is probably a higher boundary for vertical deviatoric stresses in the central part of ice shelves (away from lateral friction, ice streams convergence, rifts and crevasses suturing). This perspective is important in view of results from the deformation behavior of meteoric ice at low stresses (see e.g. Montagnat and Duval, 2004; Schulson and Duval, 2009) and references therein), where the n parameter of Glen's flow law is different and closer to 2. Similarly, it is possible that the response of the E_* parameter to its driving factors might also differ at low stress. It should therefore be beneficial to run further marine ice deformation experiments at very low stress, to extend the validity of the present data set.

Our data set demonstrates the validity of the new updated Cuffey and Paterson (2010) deformation/applied stress relationship for ice, and that newly formed marine ice can be considered as the lower boundary of the possible viscosities for natural isotropic ice across the temperature range. This therefore suggests that the lower viscosities invoked for marine ice in inverse modeling exercises mainly results from changes in the temperature field (warmer marine ice embedded in colder meteoric ice) rather than in a specific enhancement factor resulting from the intrinsic properties of marine ice. Theoretical considerations and field observations (e.g. Craven et al., 2009) indeed show that temperature profiles considerably depart from the expected linear gradient when marine ice bottom accumulation occurs below meteoric ice in significant amounts. Marine ice is often mistaken for what is referred to as the "ice mélange" in rifts and open crevasses at the surface of the ice shelf. Marine ice is indeed only one potential component of the "ice mélange" which is a composite of various ice types such as fallen meteoric ice blocks, sea ice or snow and firn, with an expected lower homogeneity and coherence. This difference in filling materials could be responsible for the contrasts in

the rheological behaviour of rifted areas in ice shelves, as discussed by Rignot and McAyeal (2008) for the Lassiter Coast and the Hemmen ice Rise at the two geographical extremes of the Filchner-Ronne Ice Shelf front. Rifts mainly filled with marine ice bodies would show a coherent rheological behaviour with the surrounding ice shelf while this would lessen or not be the case for rifts filled with an "ice mélange".

<u>Marine influence of major outlet glaciers feeding into RBIS</u>

The coastal region of Dronning Maud Land (DML), East Antarctica, has numerous outlet glaciers feeding into ice shelves that extend more than 1000 km along the coast (Figure 20). Hence, dynamic coupling between the (semi-) continuous ice shelves along the DML coast may transfer local perturbations into a wider spatial context. The West Ragnhild Glacier has a distinct tributary (flowing >10 m/a) extending about half the distance from the coast to Dome Fuji, which may allow this glacier to act as a channel that rapidly transfers dynamic changes in the DML coast to the deep interior of the East Antarctic Ice Sheet. Mass outflux from West Ragnhild Glacier (13-14 Gt/a) constitutes roughly 10% of that from DML (Rignot et al., 2008).
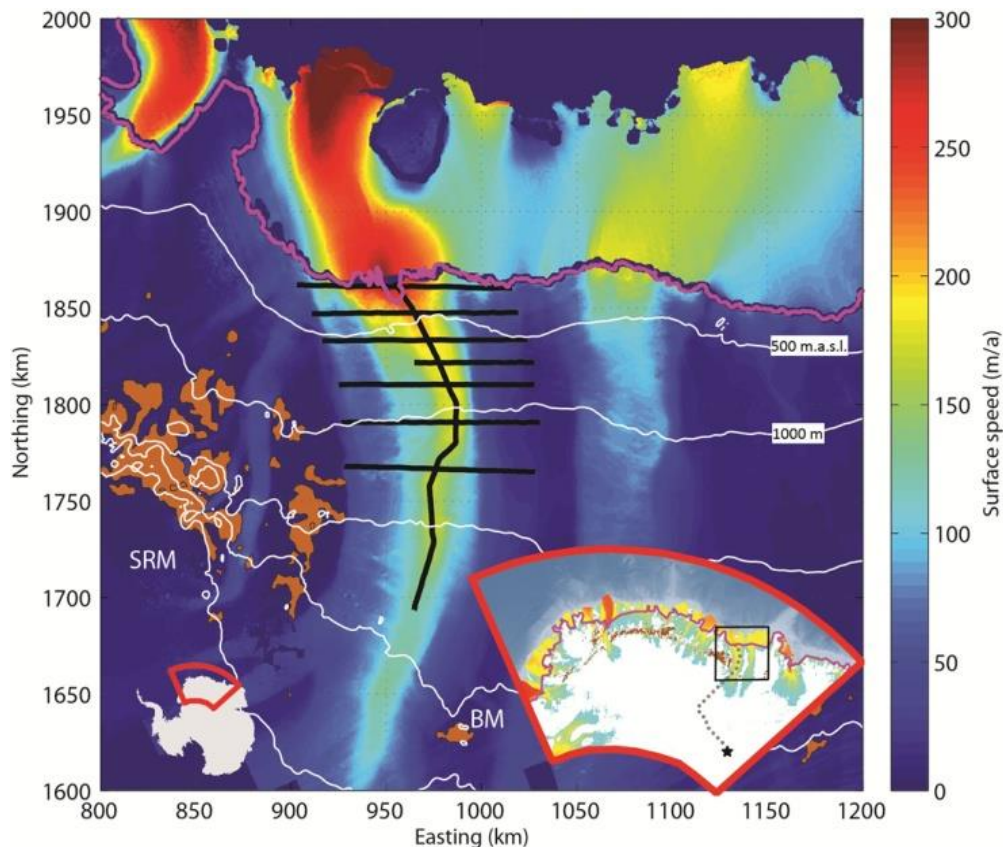

Figure 20: The West Ragnhild Glacier, Dronning Maud Land (DML), East Antarctica. Background color of the main map shows the surface flow speed derived with satellite interferometry techniques. The contours show surface elevations at 500-m intervals (Bamber et al., 2009). The grounding line is shown as purple (Bindschadler et al., 2011). Black curves show one radar profile along the center flowline of the glacier and seven across-flow profiles made for this study. Outcrops are shown as brown. Two inset maps show the coverage of the larger maps. In the lower-right inset, ice-flow speed is shown with a logarithmic scale (white, when < 15 m/a) (Rignot et al., 2011) to highlight glaciers, together with the grounding line (purple), outcrops (brown), and West Ragnhild flowline (gray dashed) towards Dome Fuji (star). The square shows the 400 km by 400

In the framework of an FP7 EUFAR project linked to the BELISSIMA project, AWI collected a series of airborne radar data on the West Ragnhild Glacier. The data show that the glacier bed makes a distinct transition from a smooth, flat, sediment-covered bed in the seaward 60-65 km to a deep valley further inland. Ice-flow modelling and satellite remote sensing show that basal motion dominates in the downstream sediment basin. We argue that the relative lack of topographic controls, the soft-bed region, and the marine termination of the West Ragnhild Glacier indicate volatility along the DML coast.
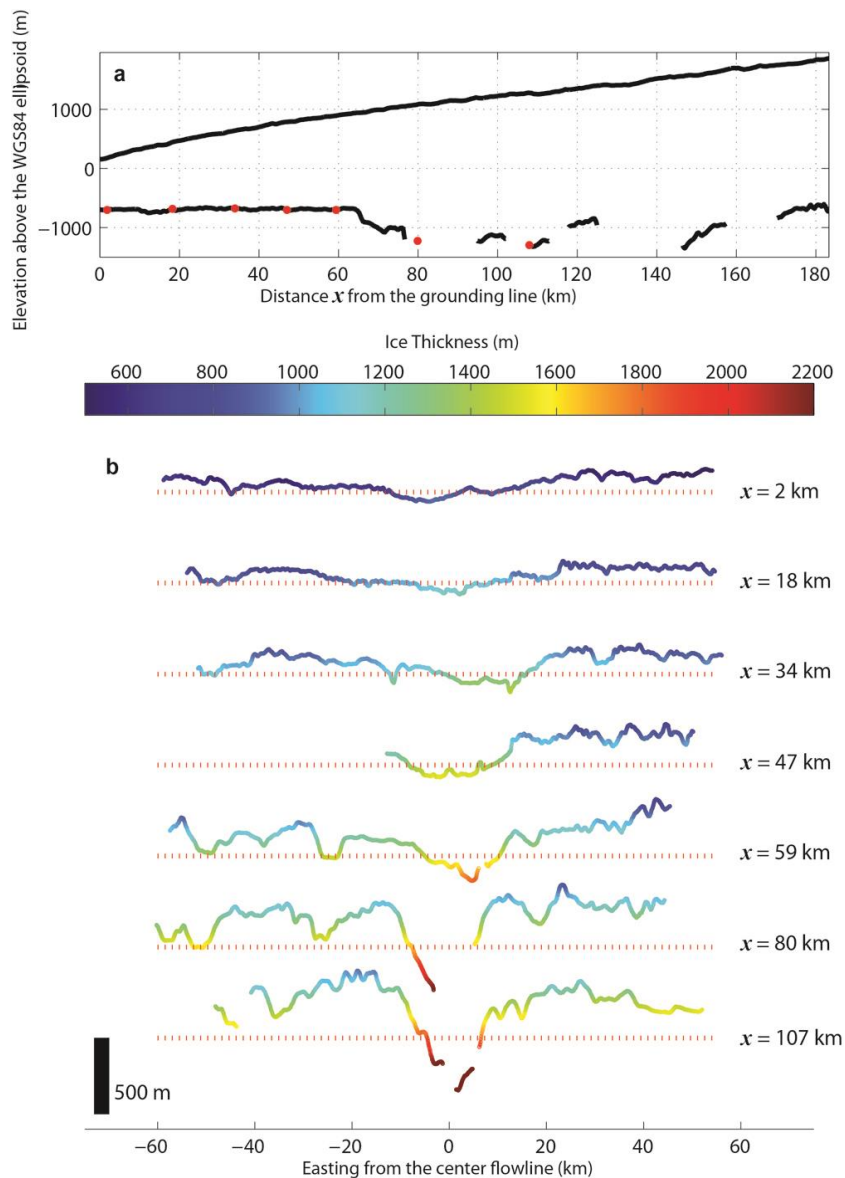
Figure 21: Radar data. (a) Ice and bed topography along the central flowline. The seven red circles are the locations of the across-flow profiles. (b) Bed topography (ordinate) and ice thickness (colour) measured across the flow. The red dotted lines show 600 m b.s.l., the approximate elevation of the flat basin measured along the centre flowline (a) and the reference for each profile. Distances of each across-flow profile (right) is measured from the grounding line.

The airborne radar surveys were done along and across the glacier using a 150-MHz radar system (Nixdorf et al., 1999; Steinhage et al., 2001). We identified the bed echo along 91% of the entire profile (Figure 21). As most sections without a bed echo are shorter than ~10 km (maximum data gap is 20 km), we speculate that these portions correspond to narrow subglacial valleys. Ice thickness was derived using a constant radio-wave propagation speed of 168 m/μs.

This survey highlights a contrast in the bed topography between seaward and landward. Figure 21 shows that the glacier bed lies ~600 m b.s.l. and is mostly flat ($\pm$ ~50 m) within ~65 km of the present-day grounding line, which makes this glacier marine terminating. Immediately landward of this flat basin, the bed slopes 300-m lower over 10 km, and this slope seems to continue further inland. The three most downstream across-flow profiles within ~35 km of the grounding line show that the bed is also smooth perpendicular to the current flowline. Therefore, there are no strong topographic constraints of the glacier outlet position. Such a bed slope, with the absence of lateral buttressing, yields in an inherent instability of the grounding-line position (Schoof, 2007). Upstream, the glacier overlies a deeply incised valley, ~20 km wide and ~1.1 km deep at two uppermost across-flow profiles.

Along these profiles, spectrum analysis of the bed topography shows that, over 1-25 km wavelengths, the seaward flat basin is distinctly smoother than the landward valley basin. As similar analyses indicate (Bingham and Siegert, 2009; Siegert et al., 2004), the downstream flat basin is likely sediment covered. Complete deglaciation over the flat basin and subsequent glacio-isostatic rebound would keep the bed well below the sea level (~500 m b.s.l.), suggesting that sediments covering the flat basin are of marine origin.

Therefore, we hypothesize that basal motion over the sediment-covered basin is significant, with the sediment acting as a soft bed. In contrast, the landward ice in the valley has little basal motion. To test this hypothesis, we next examine flow characteristics using an ice-flow model and assess subglacial conditions by analysing the radar power returned from the bed.

Interferometric analysis of satellite synthetic-aperture radar data shows that the ice accelerates steadily towards the grounding line (Figure 22a). To estimate the contribution from basal motion, we modelled the ice deformation diagnostically (i.e., steady state for present-day conditions) along the center flowline (shown in Figure 20) using a higher-order flowline model (Pattyn, 2002; Pattyn et al., 2005; 2006).

The ice flow model accounts for longitudinal and shear stresses in a two-dimensional plane along the centre flowline shown in Figure 20. The ice and bed topography within the survey domain are taken from the data collected in the framework of the EUFAR project. Beyond it, the bed and ice topography are taken from the BEDMAP dataset (Lythe et al., 2001) and from Bamber et al. (2009). To ease the flow modelling, the ice topography is relaxed to remove small-scale surface features, which does not affect large-scale flow fields. Short gaps of the bed echoes within the survey domain are interpolated linearly; such gaps are typically less than several local ice thicknesses, so details of the bed topography do not affect the large-scale flow fields. The surface mass balance is set to the present value (Van de Berg et al., 2006). The ice-flow speed at the

upper boundary of the modelled domain is set to zero (ice-flow divide) and at the grounding line satellite-measured value. The predicted large increase of the ice deformation within ~10 km of the grounding line (Figure 22a) is caused by the downstream boundary condition; that is, the modelled rapid increase of the ice deformation is an artefact, but it implicitly indicates that basal motion is significant near the grounding line.
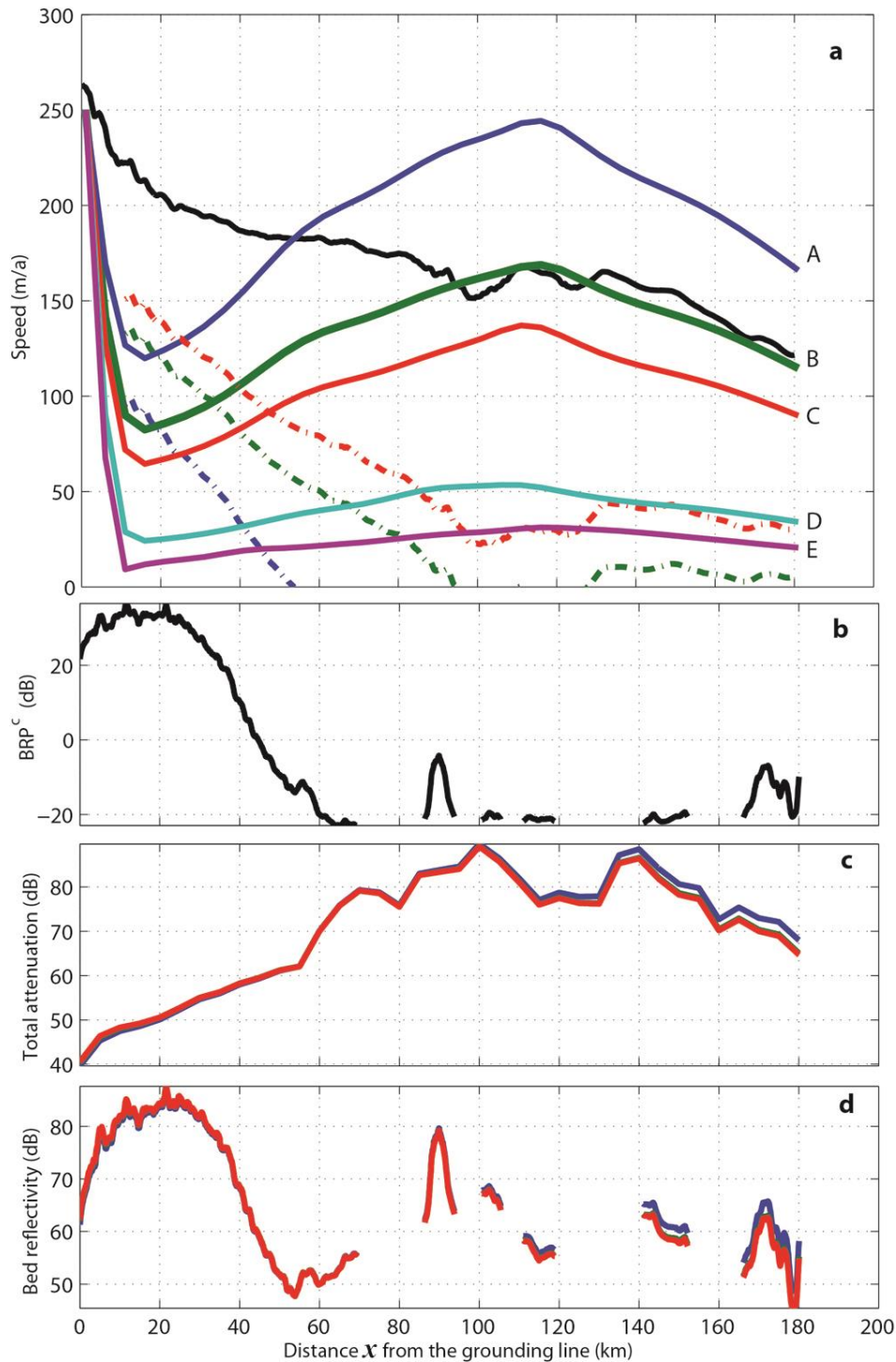
Figure 22: Flow characteristics and subglacial conditions along the center flowline. (a) Surface motion measured with satellite interferometric techniques (black). A-E mark five modelled cases of ice deformation with different flow parameters. Dashed curves are the basal motions estimated as the differences between the surface motion and ice deformation for cases. (b) Geometrically corrected bed-returned power BRPc. (c) Englacial attenuation L modelled with ice temperatures for the flow fields from cases A, B, and C. (d) Bed reflectivity R. The colours for the curves in (c) and (d) are the same as those for (a).

In the model, we defined basal motion as the difference between satellite-measured surface motion and modelled ice deformation. We took this approach because the basal-sliding law and its constraints are not well known in this area. A similar approach was taken in Recovery and Slessor basins (Rippin et al., 2003). In our ice-deformation model, the ice is assumed isothermal and flow fields are calculated for five temperature-dependent flow parameters. The model was run for five flow parameters, which correspond to ice temperatures of -2, -4, -5, -10, and -15 °C (Cuffey and Paterson, 2010). In each model run, a uniform flow parameter is used, making the ice isothermal. Thermo-mechanical coupling is unfeasible for this glacier because of numerical instability of the model, especially with respect to the vertical velocity field. This is presumably because the present-day ice topography is so different from a steady state.

Amongst the five cases, case A corresponds to the warmest (softest) ice, and predicts ice deformation slightly larger than the surface motion in the upstream region. Due to limitations from restricting our model to two dimensions, we judge that ice deformation predicted with case A is likely. Cases B and C show along-flow deformation patterns similar to case A and better replicate the surface motion in the upstream region (>100 km), so they are also likely. Cases D and E correspond to much colder (stiffer) ice and predict nearly uniform deformation in the surveyed domain, which is much smaller than the surface motion. These colder cases predict that basal motion (> 10 m/a) accounts for more than half of the surface motion within 360 km of the grounding line (Rignot et al., 2011). Such an extent makes cases D and E unlikely. All likely predictions from cases A, B, and C consistently show that the basal motion is significant in the sediment basin but its onset position depends on the case.

To further examine the spatial distribution of the basal motion, we analyzed radar power returned from the bed, hereafter BRP. The geometrically corrected bed returned power BRPc can be calculated with the radar-measured power BRP returned from the bed and the geometric factor $\left(h + \frac{d}{n}\right)^2$. Here h is the height of the airplane above the glacier surface, d is the depth, and n is the refraction index of the ice (~1.8) (e.g., Matsuoka et al., 2012). The BRP in Figure 22b is normalized to the mean of the observed values. BRP is affected by the englacial attenuation L and the bed reflectivity R . In decibel scale $([x]dB = 10log10(x)$), this relationship can be written as $[BRPc]dB = [BRP]dB + 10log10((h + d/n)^2 \simeq [R]dB - [L]dB$; effects of temporal changes in the instrumental characteristics and of ice-crystal alignments are ignored here. Englacial attenuation has contributions from pure ice and chemical constituents included in the glacier ice, both of which depend exponentially on ice temperature. Although the chemical contribution to attenuation can nearly equal the pure-ice contribution near the coast (Matsuoka et al., 2012), we ignore its contribution here and use only the pure-ice contribution.

Temperature fields associated with the steady-state flow fields are estimated using a geothermal flux of 42 mW/m², a typical value for Precambrian rocks. The geothermal flux under the glacier is probably a bit higher (50 - 60 mW/m²) (Fox-Maule et al., 2005; Shapiro and Ritzwoller, 2004), but even with the lower value of 42 mW/m², the bed in the surveyed domain is predicted to be at the pressure melting point everywhere. Once the bed reaches the pressure melting point, additional geothermal and shear heat has

virtually no effects on the ice temperature and thus also on the englacial attenuation (Matsuoka, 2011). Therefore, the estimated along-flow patterns of the attenuation and bed reflectivity are robust regardless of the uncertainties in the temperature fields.

Modelled temperature fields and Equations 3, 4, and 5 of Matsuoka et al. (2012) and parameters presented therein are used to estimate the attenuation L. Larger attenuation occurs in the inland region (Figure 22c) because ice is thicker and the depth-averaged, one-way attenuation rate $<N> (= [L]dB/(2H)$, where H is local ice thickness) monotonically increases from the grounding line (13 dB/km, one way) to the uppermost part of the survey domain (21 dB/km). The observed 60-dB variation in BRPc at 40-60 km from the grounding line (Figure 22b) is equivalent to vary $<N>$ by 150 dB/km, which is certainly an overestimate (Matsuoka et al., 2012].

The geometrically corrected BRP, BRPc, can be a proximial bed reflectivity if englacial attenuation remains unchanged (Matsuoka, 2011). In the upstream valley, Figure 3b shows that BRPc remains relatively low (-10 dB) and varies little ($\pm$10 dB) except at two sites where BRPc shows anomalous features. In these features, BRPc increases by $\sim$50 dB along a 20 km segment of data, over which the ice thins only $\sim$200 m.

All likely cases A, B, and C predict nearly identical attenuation (Figure 22c). Attenuation decreases $\sim$20 dB within 10 km around 65 km from the grounding line. Then, attenuation gradually decreases by 20 dB over 50 km. The corresponding estimated bed reflectivity rapidly increases, approaching the grounding line at 40-50 km, then varies little within the last $\sim$30 km (Figure 22d). The observed contrast in the bed reflectivity ($\sim$30 dB) is presumably due to both variations in the subglacial water amount and in the bed smoothness over one radio wavelength ($\sim$1.2 m; Peters et al., 2005). The radar-data-inferred increase in water content and bed smoothness in the sediment basin agrees with the model-predicted increase in the basal motion.

The Raymond effect and the stability of ice rises in RBIS

In one of the first numerical studies of ice divides, Raymond (1983) showed that non-Newtonian effects give rise to a mechanically stiff zone of ice underneath the ridges of
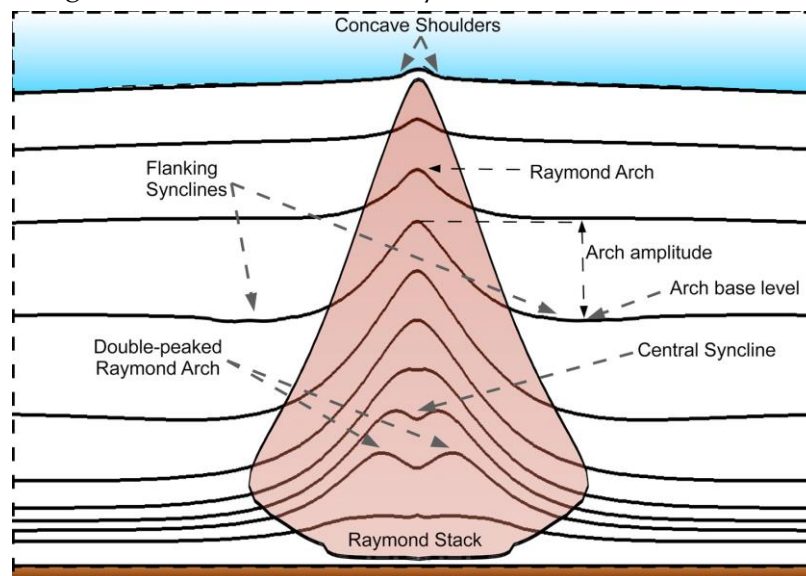

Figure 23: Cartoon illustrating terminology for stratigraphic features at ice divides. After Martín et al. (2009).

ice divides. This stiff zone of ice leads to the formation of anticlines, i.e., an upward wrapping of isochrones. These anticlines, now generally referred to as Raymond bumps, were subsequently found in radargrams collected at ice divides (e.g., Nereson et al., 1998; Vaughan et al., 1999; Conway et al., 1999). In radargrams, a vertical series of Raymond bumps are commonly seen, with one Raymond bump on the top of another forming a Raymond stack. The discovery of Raymond stacks gave an added impetus for measuring and modelling isochronal layers at ice divides (Martin et al., 2009). Figure 23 illustrates the various stratigraphical features to have been observed at ice divides, some of which arise from the nonlinear rheology of ice. It is already clear from modelling of relatively thin subtemperate ice masses that the Glen flow law cannot describe all that is seen. Martín et al. (2009) show that by considering anisotropy in ice flow, one can simulate the double arches and the size of the arch stacks, and produce plausible representations of observations. Pettit et al. (2007), using different constitutive assumptions (i.e., the relationship between the stress and strain rate tensors), reach the same conclusions regarding the relationship between arch size and anisotropic flow.

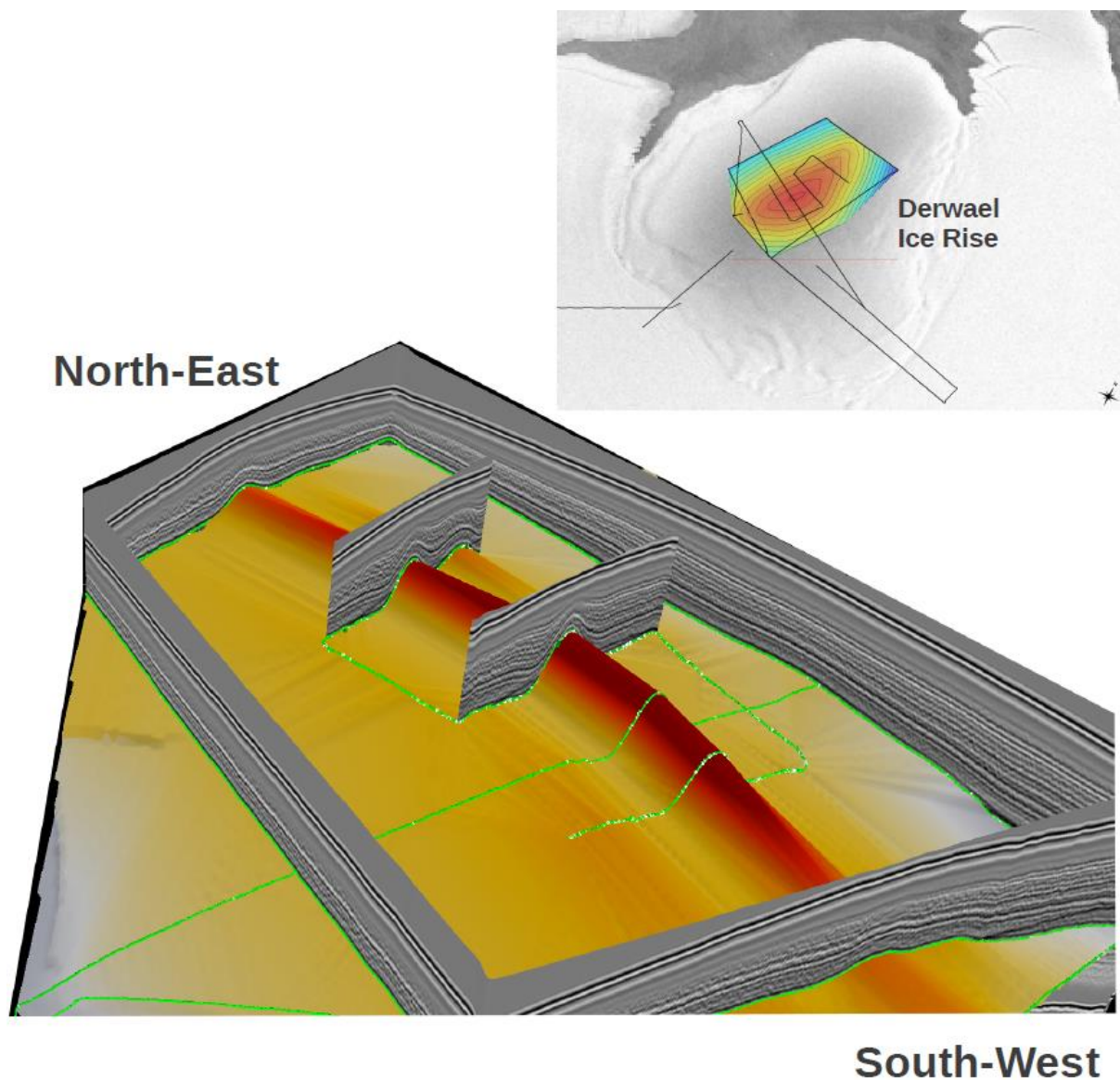
Figure 24: Radar profiles across the divide region of Derwael ice rise. The bottom image shows the depth of an isochrone layer, showing the upwarping of that layer under the ice divide due to the Raymond effect (bump in the radar reflectors).

Particularly useful in this regard is the arch amplitude, and also the height at which the maximum amplitude is reached. For a given ice rheology, these two parameters provide information about the time of formation of the divide, and whether the ice thickness at the divide has subsequently changed (Hindmarsh et al., 2011).

Data collected during BELISSIMA on Derwael ice rise (Figure 24), show a distinct Raymond bump underneath the central ice divide, which points to long-term stable conditions of the ice rise. However, radar data do not allow at this stage to fully capture the size of the complete Raymond bump. New data will however be collected in the framework of the new BELSPO sponsored IceCon project, and will be analysed for this purpose. This is also one of the main targets for this subsequent project.

Discussion

Most observations of melt rates underneath ice shelves stem from satellite altimetry (e.g., Pritchard et al., 2012). However, close to the grounding line where the ice shelf is not freely floating, ice thickness may well be overestimated using the satellite technique, leading to biases in basal melt rates. Our estimates based on measured ice thickness are not hampered by this bias and therefore more reliable and robust.

It is generally thought that high rates of sub-shelf melting such as those observed on the Pine Island shelf (20-30 m/a; Rignot 1998; Jacobs et al., 2011), and George VI Ice Shelf (2.2-2.8 m/a; Potter and Paren, 1985; Corr et al, 2002) are caused by incursions of CDW through deep troughs crossing the continental shelf and entering ice shelf cavities. More modest melting ~0.6 m/a) measured beneath the Filchner Ice Shelf has been attributed to a convective thermohaline circulation due to HSSW formation (Hellmer and Olbers, 1989; Nicholls et al., 2006). Similar melt rates of 0.85 (but up to 2.85) m/a have been measured using phase-sensitive radar near the grounding line of Rutford Ice Stream (Jenkins et al., 2006), and melt rates up to 0.85 m/a were also measured near the shore of the Fimbul ice shelf (Nicholls et al., 2006; 2008).

In contrast, our measurements across the grounding line of Roi Baudouin Ice Shelf indicate relatively small melt rates ~0.15 m/a) compared with those measured beneath large ice shelves. Tidal influences can increase the intensification of sub-shelf circulation, resulting in increased melting and refreezing (MacAyeal, 1984; Makinson et al., 2011). Local geometry of the water column beneath a shelf and tidal mixing may also be important; model simulations (Holland, 2008) show that such mixing is confined to small areas and may only become significant under near-freezing conditions where the ocean cavity slope is shallow and tidal stirring is vigorous. Although such favourable conditions do exist beneath Roi Baudouin Ice Shelf, the relatively low melt rate indicated by our model-based interpretations of the radar data (Figure 7) suggests that this mechanism is not strong.

Our observations indicate that the occurrence of accreted marine ice is restricted primarily to the rift zone. In such areas, it is thought that melt-driven convection at the sides of a rift cause cavity water to ascend and supercool, resulting in marine ice formation (Khazendar and Jenkins, 2003). Khazendar (2000) has also shown that the amount of ice accreted in such rifts is greatly increased by the presence of pre-existing ISW formed upstream. Moreover, the CTD profiles collected from boreholes near the

edge of the shelf, downstream from the rift suggest that a weak outflow of shallow ISW is present.

The weak melting at the grounding line implies a weak buoyancy-forced circulation and correspondingly low freezing rates (i.e. a weak ``ice pump''). Also the ice front region could easily be influenced by downwelling of the seasonally warmer surface layer (Hattermann et al., 2012). Even if all the cavity waters were all at the surface freezing point, basal freezing may only influence the outer part of the ice shelf near the ice front (Lane-Serff, 1995), and marine ice could be melted off by downwelling beneath the ice front, leaving only marine ice in the rifts where it is protected.

The incursion of HSSW or the downwelling of the seasonally warmer surface layer rather than CDW beneath the eastern RBIS is most probably controlled by regional water mass flows combined with RBIS' shallow sub-shelf cavity. Since other ice shelves in the sector appear to be underlain by similarly shallow cavities, as evidenced by shelf-edge bathymetric data and the presence of frequent ice rises along the Princess Ragnhild Coast, it is likely that similar conditions might well prevail more widely than at RBIS alone (e.g., Hattermann et al., 2012). Thus, we postulate that many of the ice shelves in this sector of East Antarctica are characterized by sub-shelf water circulation systems that are dominated by either the incursion of HSSW or the downwelling of ASW and characterized by low levels of sub-shelf melting and freezing relative to larger shelf systems located elsewhere in Antarctica. The shallowness of the bathymetry in this area is restricted to the sections close to ice rises and ice-rise promontories. Deeper troughs at the exit of large outlet glaciers feeding into RBIS and other ice shelves in this sector of DML do exist and seem to exhibit a different type of ice/ocean interaction.

For the Western Ragnhild Glacier, feeding into the RBIS, the grounding line location is relatively well constrained by both ice-penetrating radar (sudden slope break in the bottom profile of the ice, Figure 16) and satellite imagery (Bindschadler et al., 2011). Upstream of the grounding line, Western Ragnhild Glacier is characterized by a flat-lying bed extending approximately 60km up-flow and lying at an average depth of approximately 700m b.s.l. (Figure 16 and 17). Although we have no direct evidence for its origin, such a smooth flat surface is characteristic of the presence of marine sediments (Bingham and Siegert, 2009), bearing witness to prior regressions of the grounding line.

Western Ragnhild Glacier is a major outlet glacier draining a significant portion of the East-Antarctic ice sheet, comprising the flow diverted around the Sør Rondane Mountains (Pattyn et al., 2005). High flow speeds are recorded well inland of the grounding line (Pattyn et al., 2005) that are comparable to other Antarctic ice streams. Flow speeds at the grounding line are of the order of 300 m/year, leading to a grounding line flux of approximately 9.5 Gt/year, slightly lower than the flux of two well-known outlet glaciers in this section of East Antarctica, i.e., Jutulstraumen (14.2 Gt/year; Høydal, 1996) and Shirase Glacier (13.8 Gt/year; Pattyn and Derauw, 2002). Those outlet glaciers show a significant higher flow velocity at the grounding line compared to Western Ragnhild Glacier (Shirase Glacier grounding line velocity is up to 2 km/year), due to ice flow convergence and lack of ice shelf buttressing. However, the Shirase Glacier grounding line cannot retreat any further due to bedrock topography above sea level inland. This makes Shirase Glacier rather stable, despite being identified as

sensitive to basal melting due to potential direct access of warm deep water (Rignot and Jacobs, 2002).

In contrast, Western Ragnhild Glacier is relatively wide (60km, Figure 3) and deep (mean depth of 550 m b.s.l. at the grounding line, locally reaching 750 m b.s.l. – Figure 17). The ice shelf is currently buttressed by two ice rises on either side of the central flowline (Figure 3). Nevertheless, the lack of very well defined topographical constraints in the grounded coastal stretch makes this ice stream potentially more sensitive to change (Schoof, 2007,Bingham et al., 2012). If the intrusion of warm mCDW onto the continental shelf is recent (the lack of long-term repeat measurements in Pritchard et al. (2012) prevents a thorough evaluation of ice shelf change) and accelerating, as in other regions on the Antarctic continental shelf (Jacobs et al., 2011), the change in oceanic erosion may become significant, and could easily be mimicked under other as yet-under-surveyed ice shelves along the East Antarctic continental margin.

Other outlet glaciers in DML similarly discharge into the low, relatively flat basin, with similarly weak constraints to the glacier outlet positions (Fretwell et al., 2012). These low beds underneath the other glaciers may also be sediment covered and act as a soft bed. The lack of lateral constraints plus the marine termination sloping downward and inland increase the instability of the grounding line along the DML coast (Schoof, 2007). The close proximity of the DML ice shelf to the margin of the continental shelf (Timmermann et al., 2010) could potentially allow relatively warm water from the abyssal plains to circulate under the shelf, leading to greater sub-shelf melting, as shown before.

Though the Roi Baudouin Ice Shelf, downstream of the West Ragnhild Glacier, has relatively weak ice/ocean interactions recently (Pattyn et al., 2012) and the present-day DML ice sheet is nearly in balance (Rignot et al., 2008), the combination of the geographic settings that we report here indicate that DML has more potential for dramatic ice-ocean interaction than previously thought. Further study of their characteristics and controls of the inter-connected system of outlet glaciers and ice shelves in DML may also help us understand a system like the Transantarctic Mountains and the grounded Ross Ice Shelf during glacial periods in which valley glaciers fed into the low, flat basin currently under the ice shelf.

Conclusions

Ice-penetrating radar and kinematic GPS surveys across a grounding line, and ice core drilling within a zone of rifting farther downstream reveal sub-ice shelf melting near the grounding line and limited accretion of marine ice in the rift zone. The rate of sub-ice shelf melting is 0.15 m/a, which is rather low for an Antarctic ice shelf. Marine ice accretion is found in a rift system close to the edge of the ice shelf where it is either formed locally or protected from melting due to warmer surface waters near the shelf edge. We conclude that the weak melt rates at the grounding line are not sufficient to sustain large-scale accretion of marine ice. We suspect that similar weak melting/refreezing conditions occur along much of the coastal sector in Dronning Maud Land where ice shelves are interspersed by ice rises and where rifting commonly occurs between those ice rises and the shelf front.

However, we also found the first evidence in East Antarctica of modified circumpolar deep water (mCDW) with significant warmth on the continental shelf, in the central part of the ice shelf, where a large outlet glacier (Western Ragnhild Glacier) feeds into. This warm mCDW can access the grounding line of the East Antarctic Ice Sheet (EAIS) through a deep trough in the continental shelf. This water is 1.7 degrees warmer than the in-situ freezing temperature at depth and was found at a depth range indicating it potentially enhances sub-shelf melting near the grounding line of Western Ragnhild Glacier, one of the most distinct fast-flowing glaciers in Dronning Maud Land. Western Ragnhild Glacier is grounded well below sea level with a bedrock slope that is close to zero. This setting suggests that inland grounding-line retreat may occur in response to oceanic perturbations. The current relatively slow ice velocity at the grounding line of 300 m/year is due to an important buttressing effect of two ice rises pinning the ice shelf (Favier et al., 2012). Increased melting and subsequent unpinning could lead to rapid, significant grounding line retreat and ice mass loss.

3. POLICY SUPPORT

The BELISSIMA project allowed Belgian glaciological activities to further develop and improve their experimental and modelling tools to study a complete new part of the Antarctic ice sheet, as part of the installation of the new Princess Elisabeth Antarctica facility recently established. This project has also enabled to have the glaciological teams to contribute to on-going national and international scientific and policy-relevant efforts.

Recent evidence shows that major changes in the Antarctic ice sheet on time scales of decades (and not of thousands of years) are due to direct interaction with the ocean through sub-ice shelf melting and loss of buttressing, and not due to short-term changes in surface mass balance. Precise knowledge of the current and future mass balance of the Antarctic ice sheet is therefore closely related to the understanding of the processes that occur at this interface. The outcome of the BELISSIMA project has directly contributed to EU FP7 programmes, such as ice2sea, and results have been fed into the IPCC AR5 draft report.

Finally, the BELISSIMA project has allowed Belgian teams to keep a glaciological research potential operational to be able to perform scientific work out of the Princess Elisabeth Station, and this also contributes to the objectives of Belgian science policy.

4. DISSEMINATION AND VALORISATION

Members of the BELISSIMA team participated in many of the most important national and international conferences to present the results of their work and to act as session convenors. A non-exhaustive list of the meetings attended by ASPI members included all of the annual meetings of the European Geosciences Union (EGU), most of the fall meetings of the American Geophysical Union (AGU), most of the international symposia organised by the International Glaciological Society (IGS), many of the meetings organised by the Scientific Committee of Antarctic Research (SCAR) and by the International Association of Cryospheric Sciences (IASC), amongst several others. The international embedding with foreign project partners fortifies the links between different institutions and polar facilities. PhD students (e.g. D. Callens) were therefore

enabled to complete their PhD in a broader internationally embedded context and wider support. This was made possible by the intensive collaborations and exchanges due to BELISSIMA. BELISSIMA members could therefore also participate in foreign polar research programmes, such as the Norwegian Polar Programme.

At the national level, members of the BELISSIMA team were interviewed regularly for radio, newspapers, and television. On a regular basis, invitations were accepted for talks for a wider audience in schools, organisations and as part of the outreach programmes of our universities.

In addition, the main research results of the BELISSIMA team were published in 6 peer-reviewed papers resulting directly from the project.

5. PUBLICATIONS

A1 publications

Callens, D., K. Matsuoka, D. Steinhage, B. Smith, F. Pattyn (submitted) Evidence for soft-bedded, marine-terminating outlet glaciers in East Antarctica.

Dierckx, M. and Tison, J.-L. (2013). Marine ice deformation experiments: an empirical validation of creep parameters. GRL, XX, 1-5, doi:10.1029/2012GL054197.

Hubbard, B., J.L. Tison, F. Pattyn, M. Dierckx, T. Boereboom, D. Samyn (2012) Optical-televiewer-based identification and characterization of material facies associated with an ice-shelf rift. Ann. Glaciol. 53(60): 53 (60), 137-146

Leonard, K., F. Pattyn, D. Callens, K. Matsuoka, J.J. Derwael, J.L. Tison (submitted) Warm deep water under an East Antarctic ice shelf: implications for grounding-line melt. Submitted to Nature Geoscience.

Matsuoka, K., F. Pattyn, D. Callens, H. Conway (2012) Radar characteristics of the basal interface across the grounding zone of an ice-rise promontory, East Antarctica. Ann. Glaciol. 53(60): 29-34

Pattyn, F., K. Matsuoka, J. Berte (2010) Glacio-meteorological conditions in the vicinity of the Belgian Princess Elisabeth Station, Antarctica. Antarctic Science 22 (1), 79-85, doi:10.1017/S0954102009990344

Pattyn F., K. Matsuoka, H. Conway, D. Callens, M. Depoorter, D. Docquier, B. Hubbard, D. Samyn, JL. Tison (2012) Radar and ice-core evidence for active ice-ocean interaction under the Roi Baudouin Ice Shelf, East Antarctica. J.Geophys. Res.117, F04008, doi:10.1029/2011JF002154.

Abstract publications

Depoorter, M., Samyn, D., Hubbard, B., Pattyn, F., Matsuoka, K., Dierckx, M. and Tison, J.-L., 2010. Investigating the "ice mélange" in an ice shelf coastal rift along the Princess Ragnhild Coast (Antarctica), Geophysical Research Abstracts, Vol. 12, EGU2010-911-1.

Hubbard, B., J.L. Tison, D. Samyn, F. Pattyn, K. Matsuoka. 2010. Optical televiewer imaging of ice facies within and around an Antarctic ice shelf rift, Geophysical Research Abstracts, Vol. 12, EGU2010-5587.

Matsuoka, K., H. Conway, D. Samyn, M. Depoorter, B. Hubbard, JL. Tison, and F. Pattyn. 2010. Radar-observed structures of interior and bottom of an ice shelf, East Dronning Maud Land, Antarctica, Geophysical Research Abstracts Vol. 12, EGU2010-7432.

Pattyn F., K. Matsuoka, D. Docquier, D. Callens, H. Conway. 2010. The role of ice rises in the stability of an ice sheet: a forward/inverse approach to interpret radar layers using ice-flow models. Geophysical Research Abstracts Vol. 12, EGU2010-11651

6. ACKNOWLEDGEMENTS

7. REFERENCES

Bamber, J. L., J. L. Gomez-Dans, and J. A. Griggs (2009), A new 1 km digital elevation model of the antarctic derived from combined satellite radar and laser data—Part 1: Data and methods, Cryosphere, 3(1), 101–111.

Bindoff, NL, MA Rosenberg, MJ Warner (2000) On the circulation and water masses over the Antarctic continental slope and rise between 80 and 150°E, Deep-Sea Research II, 47, 2299-2326

Bindschadler, R. A., H. Choi, and ASAID Collaborators (2011), High-Resolution Image-derived Grounding and Hydrostatic Lines for the Antarctic Ice Sheet, http://nsidc.org/data/docs/agdc/nsidc0489_bindschadler/index.html, Natl. Snow and Ice Data Cent., Boulder, Colo.

Bingham RG et al (2012) Inland thinning of West Antarctic Ice Sheet steered along subglacial rifts, Nature 487, doi:10.1038/nature11292

Bingham, RG and MG Siegert (2009) Quantifying subglacial bed roughness in Antarctica: implications for ice-sheet dynamics and history. Quaternary Science Reviews 28, 223-236

Budd W.F. and Jacka T. H. (1989), A review of ice rheology for ice sheet modelling, CRST, 16(2), 107–144

Catania, G. A., C. Hulbe, and H. Conway (2010), Grounding line basal melt rates from radar-derived internal stratigraphy, J. Glaciol., 56(197), 545–554.

Catania, G. A., H. Conway, C. F. Raymond, and T. A. Scambos (2006), Evidence for floatation or near floatation in the mouth of Kamb Ice Stream, West Antarctica, prior to stagnation, J. Geophys. Res., 111, F01005, doi:10.1029/2005JF000355.

Conway, H., B. Hall, G. Denton, A. Gades, and E. Waddington (1999), Past and future grounding-line retreat of the West Antarctic ice sheet, Science, 286, 280–283.

Corr, H. F. J., A. Jenkins, K. W. Nicholls, and C. S. M. Doake (2002), Precise measurement of changes in ice-shelf thickness by phase-sensitive radar to determine basal melt rates, Geophys. Res. Lett., 29(8), 1232, doi:10.1029/2001GL014618.

Corr, H., M. Popple, and A. Robinson (1995), Airborne radio echo investigations of a marine ice body, Filchner-Ronne Ice Shelf Progr. Rep. 8, pp. 14–17, Alfred Wegener Inst. for Polar and Mar. Res., Bremerhaven, Germany.

Craven, M., F. Carsey, A. Behar, J. Matthews, R. Brand, A. Elcheikh, S. Hall and A. Treverrow 2005. Borehole imagery of meteoric and marine ice layers in the Amery Ice Shelf, East Antarctica. *Journal of Glaciology*, **51**(172): 75-84.

Craven, M., I. Allison, H.A. Fricker and R. Warner 2009. Properties of a marine ice layer under the Amery Ice Shelf, East Antarctica. *Journal of Glaciology*, **55**(192): 717-728.

Cuffey K. M. and Paterson W. S. B. (2010), The Physics of Glaciers, fourth edition, Oxford, Butterworth-Heinemann, 693 p.

Cuffey, K. M., and W. S. B. Paterson (2010), The Physics of Glaciers.

Derwael, JJ (1985) Levés Altimétriques - BRB - Côte Princesse Ragnild, Expéditions Antarctiques Belgo-Néerlandaises (5 maps), Exantar.

Dierckx M., Goossens T., Samyn D. and Tison JL (2010), Compression experiments on artificial, alpine and marine ice: Implications for ice-shelf/continental interactions, Geophys. Res. Abstr., Vol. 12, 761

Dowdeswell, JA, J Evans, C O'Cofaigh, JB Anderson (2006) Morphology and sedimentary processes on the continental slope off Pine Island Bay, Amundsen Sea, West Antarctica. Geological Society of America Bulletin, v. 118, p. 606-619

Dupont, T. K., and R. B. Alley (2005), Assessment of the importance of ice shelf buttressing to ice-sheet flow, Geophys. Res. Lett., 32, L04503, doi:10.1029/2004GL022024.

Favier, L, O Gagliardini, G Durand, T Zwinger (2012) A three-dimensional full Stokes model of the grounding line dynamics: effect of a pinning point beneath the ice shelf, The Cryosphere 6(1), 101-112.

Feltham, D.L., N. Untersteiner, J.S. Wettlaufer and M.G. Worster 2006. Sea ice is a mushy layer. *Geophysical Research Letters*, **33**(14): L14501.

Fox-Maule, C., et al. (2005), Heat flux anomalies in Antarctica revealed by satellite magnetic data, Science, 309(5733), 464-467.

Fretwell, P., et al. (2012), Bedmap2: improved ice bed, surface and thickness datasets for Antarctica, The Cryosphere Discuss., 6(5), 4305-4361.

Fricker, H. A., S. Popov, I. Allison, and N. Young (2001), Distribution of marine ice beneath the Amery Ice Shelf, Geophys. Res. Lett., 28(11), 2241–2244.

Fujita, S., H. Maeno, S. Uratsuka, T. Furukawa, S. Mae, Y. Fujii, and O. Watanabe (1999), Nature of radio echo layering in the Antarctic ice sheet detected by a two-frequency experiment, J. Geophys. Res., 104(B6), 13,013–13,024

Gagliardini, O., G. Durand, T. Zwinger, R. C. A. Hindmarsh, and E. L. Meur (2010), Coupling of ice-shelf melting and buttressing is a key process in ice-sheet dynamics, Geophys. Res. Lett., 37, L14501, doi:10.1029/2010GL043334.

Glen J. W. (1958), The flow law of ice: A discussion of the assumptions made in glaciers theory, their experimental foundations and consequences, IASH, 171–183.

Gough, AJ, AR Mahoney, PJ Langhorne, MJM Williams, NJ Robinson, TG Haskell (2012) Signatures of supercooling: McMurdo Sound platelet ice, Journal of Glaciology 58 (207), doi: 10.3189/2012JoG10J218

Gow, A. J., and S. Epstein (1972), On the use of stable isotopes to trace the origins of ice in a floating ice tongue, J. Geophys. Res., 77(33), 6552–6557.

Greve, R. (1997), Large-scale ice-sheet modelling as a means of dating deep ice cores in Greenland, J. Glaciol., 43(144), 307–310.

Haefeli, R. (1963), A numerical and experimental method for determining ice motion in the central parts of ice sheets, IAHS Publ., 61, 253–260.

Hattermann, T., O. A. Nøst, J. M. Lilly, and L. H. Smedsrud (2012), Two years of oceanic observations below the Fimbul Ice Shelf, Antarctica, Geophys. Res. Lett., 39, L12605, doi:10.1029/2012GL051012.

Hawley, R.L. and E.M. Morris 2006. Borehole optical stratigraphy and neutron-scattering density measurements at Summit, Greenland. *Journal of Glaciology*, **52**(179): 491-496.

Hawley, R.L., E.D. Waddington, R.B. Alley and K.C. Taylor 2003. Annual layers in polar firn detected by Borehole Optical Stratigraphy. *Geophysical Research Letters*, **30**(15).

Hellmer, H. H., and D. J. Olbers (1989), On the thermohaline circulation beneath the Filchner-Ronne ice shelves, Antarct. Sci., 3(4), 433–442.

Hindmarsh, R. C. A. (1999), On the numerical computation of temperature in an ice sheet, J. Glaciol., 45(151), 568–574.

Holland, DM, and A Jenkins (1999) Modelling thermodynamic ice-ocean interactions at the base of an ice shelf. J. Phys. Oceanogr., 29, 1787-1800

Holland, P. R. (2008), A model of tidally dominated ocean processes near ice shelf grounding lines, J. Geophys. Res., 113, C11002, doi:10.1029/2007JC004576.

Hooke R. L.. (1998), Principles of Glacier Mechanics, Upper Saddle River, N. J.: Prentice Hall, 248 p.

Høydal, ØA (1996) A force-balance study of ice flow and basal conditions of Jutulstraumen, Antarctica. J. Glaciol. 42 (142), 413–425.

Hubbard, B., J. L. Tison, F. Pattyn, M. Dierckx, T. Boereboom, and D. Samyn (2012), Optical televiewer-based identification and characterization of material facies associated with an Antarctic ice-shelf rift, Ann. Glaciol., 53(60), 137–146.

Hubbard, B., S. Roberson, D. Samyn and D. Merton-Lyn 2008. Digital optical televiewing of ice boreholes. *Journal of Glaciology*, **54**(188): 1-8.

Hubbard, B., S. Roberson, D. Samyn, and D. Merton-Lyn (2008), Digital optical televiewing of ice boreholes, J. Glaciol., 54(188), 823–830.

Huybrechts, P. (1994), Formation and disintegration of the Antarctic ice sheet, Ann. Glaciol., 20, 336–340.

Iwanaga, Y and H. Yohju (1987) Oceanographic data of the 27th Japanese Antarctic Research Expedition from November 1985 to April 1986, JARE Data Reports 75 (126), 1-56

Iwanami, K and H Tohju (1987) Oceanographic data of the 26th Japanese Antarctic Research Expedition from November 1984 to April 1985, JARE Data Reports 75 (174) 1-59

Jacka T. H. (1984), The time and strain required for development of minimum strain rates in ice, CRST, 8, 261–268

Jacka T. H. and Li J.(1994), The steady-state crystal size of deforming ice, J. Glaciol., 20, 13–18

Jacobs, S. S., A. Jenkins, C. F. Giulivi, and P. Dutrieux (2011), Stronger ocean circulation and increased melting under Pine Island Glacier ice shelf, Nat. Geosci., 4, 519–523.

Jacobs, S. S., H. H. Helmer, C. S. M. Doake, A. Jenkins, and R. M. Frolich (1992), Melting of ice shelves and the mass balance of Antarctica, J. Glaciol., 38(130), 357–387.

Jacobs, SS (1991) On the nature and significance of the Antarctic Slope Front, Marine Chemistry 35, 9-24.

Jenkins, A., H. F. J. Corr, K. W. Nicholls, C. L. Stewart, and C. S. M. Doake (2006), Interactions between ice and ocean observed with phase sensitive radar near an Antarctic ice-shelf grounding line, J. Glaciol., 52(178), 325–346.

Jenkins, A., P. Dutrieux, S. Jacobs, S. McPhail, J. Perrett, A. Webb, and D. White (2010), Observations beneath Pine Island Glacier in West Antarctica and implications for its retreat, Nat. Geosci., 3(7), 468–472.

Jones S. J. and Glen J. W. (1969), The effect of dissolved impurities on the mechanical properties of ice crystals, Phil. Mag., Vol. 19, 157, 13–24

Khazendar A. (2000), Marine ice formation in rifts of Antarctic ice shelves: A combined laboratory study and modeling approach, PhD thesis, Science Faculty, Université Libre de Bruxelles, Bruxelles, Belgium

Khazendar A., Rignot E. and Larour E. (2009), Roles of marine ice, rheology, and fracture in the flow and stability of the Brunt/Stancomb- Wills Ice Shelf, J. Geophys. Res., vol. 114, F04007.

Khazendar A., Tison J.L., Stenni B., Dini M. and Bondesan A. (2001), Significant marine-ice accumulation in the ablation zone beneath an Antarctic ice shelf, J. Glaciol., vol. 47 158, 359–368

Khazendar, A. (2000), Marine ice formation in rifts of Antarctic ice shelves: A combined laboratory and modeling approach, PhD thesis, Univ. libre de Bruxelles, Brussels.

Khazendar, A. and Jenkins A. (2003) A model of marine ice formation within Antarctic ice shelf rifts. J. Geophys. Res., vol. 108(C7) 3235

Khazendar, A., and A. Jenkins (2003), A model of marine ice formation within Antarctic ice shelf rifts, J. Geophys. Res., 108(C7), 3235, doi:10.1029/2002JC001673.

Khazendar, A., J. L. Tison, B. Stenni, M. Dini, and A. Bondesan (2001), Significant marine-ice accumulation in the ablation zone beneath an Antarctic ice shelf, J. Glaciol., 47(158), 359–368.

Lane-Serff, G. F. (1995), On meltwater under ice shelves, J. Geophys. Res., 100(C4), 6961–6965.

Langway C. C. J. (1958), Ice fabrics and the Universal stage, CRREL Tech. Rep. 62, pp. 16

Lewis, E. L., and R. G. Perkins (1986), Ice pumps and their rates, J. Geophys. Res., 91(C10), 11,756–11,762.

Lythe, M. B., et al. (2001), BEDMAP: A new ice thickness and subglacial topographic model of Antarctica, Journal of Geophysical Research-Solid Earth, 106(B6), 11335-11351.

MacAyeal, D. R. (1984), Thermohaline circulation below the Ross Ice Shelf: A consequence of tidally induced vertical mixing and basal melting, J. Geophys. Res., 89(C1), 597–606.

Makinson, K., P. R. Holland, A. Jenkins, K. W. Nicholls, and D. M. Holland (2011), Influence of tides on melting and freezing beneath Filchner-Ronne Ice Shelf, Antarctica, Geophys. Res. Lett., 38, L06601, doi:10.1029/2010GL046462.

Martín, C., R. C. A. Hindmarsh, and F. J. Navarro (2009b), On the effects of divide migration, along-ridge flow, and basal sliding on isochrones near an ice divide, J. Geophys. Res., 114, F02006, doi:10.1029/2008JF001025

Martin, S. (1981), Frazil ice in rivers and oceans, Ann. Rev. Fluid Mech., 13, 379–397.

Matsuoka, K. (2011), Pitfalls in radar diagnosis of ice-sheet bed conditions: Lessons from englacial attenuation models, Geophysical Research Letters, 38.

Matsuoka, K., et al. (2012), Predicting radar attneuation within the Antarctic Ice Sheet, Earth and Planetary Science Letters.

Matsuoka, K., F. Pattyn, D. Callens, and H. Conway (2012), Radar characteristics of the basal interface across the grounding zone of an ice-rise promontory, East Antarctica, Ann. Glaciol., 53(60), 29–34.

Meijers, AJS, A Klocker, NL Bindoff, GD Williams, and SJ Marsland (2010) The circulation and water masses of the Antarctic shelf and continental slope between 30 and 80°E, Deep Sea Research II, 57, doi:10.1016/j.dsr2.2009.04.019

Meredith, MP, AC Naveira Garabato, AMcC Hogg, and R Farneti (2012) Sensitivity of the overturning circulation in the Southern Ocean to decadal changes in wind forcing, J. Climate, doi:10.1175/2011JCLI4204.1

Montagnat M. and Duval P. (2004) The viscoplastic behaviour of ice in polar ice sheets: Experimental results and modelling, C. R. Physique, 5, 699–708

Moore J.C., Reid A.P. and Kipfstuhl J. (1994) Microstructure and electrical properties of marine ice and its relationship to meteoric ice and sea ice, J. Geophys. Res., vol. 99(C3), 5171–5180

Morgan, V. (1972), Oxygen isotope evidence for bottom freezing on the Amery Ice Shelf, Nature, 238, 393–394.

Mügge, B., A. A. Savvin, R. Calov, and R. Greve (1999), Numerical age computation of the Antarctic ice sheet for dating deep ice cores, in Advances in Cold-Region Thermal Engineering and Sciences, edited by Y. W. K. Hutter and H. Beer, pp. 307–318, Springer, New York.

Nereson, N. A., C. F. Raymond, E. D. Waddington, and R. W. Jacobel (1998), Migration of the Siple Dome ice divide, West Antarctica, J. Glaciol., 44, 643–652.

Nicholls, K. W., E. P. Abrahamsen, K. J. Heywood, K. Stansfield, and S. Osterhus (2008), High-latitude oceanography using the Autosub autonomous underwater vehicle, Limnol. Oceanogr., 53(5), 2309–2320.

Nicholls, K. W., et al. (2006), Measurements beneath an Antarctic ice shelf using an autonomous underwater vehicle, Geophys. Res. Lett., 33, L08612, doi:10.1029/2006GL025998.

Nishio, F., M. Ishikawa, H. Ohmae, S. Takahashi, and T. Katsushima (1984), A preliminary study of glacial geomorphology in area between Breid Bay and the Sør Rondane Mountains in Queen Maud Land, East Antarctica, Nankyoku Shiryô, 83, 11–28.

Nixdorf, U., et al. (1999), The newly developed airborne radio-echo sounding system of the AWI as a glaciological tool, in Annals of Glaciology, Vol 29, 1999, edited by T. H. Jacka, pp. 231-238.

Nøst, O. A., M. Biuw, V. Tverberg, C. Lydersen, T. Hattermann, Q. Zhou, L. H. Smedsrud, and K. M. Kovacs (2011), Eddy overturning of the Antarctic Slope Front controls glacial melting in the Eastern Weddell Sea, J. Geophys. Res., 116, C11014, doi:10.1029/2011JC006965.

Oerter H., Kipfstuhl J., Determann J., Miller H., Wagenbach D., Minikin A. and Graf W. (1992) Evidence for basal marine ice in the Filchner-Ronne Ice Shelf. Nature, vol. 358 6385, 399–401

Oerter, H., J. Kipfsthül, J. Determann, H. Miller, D. Wagenbach, A. Minikin, and W. Graf (1992), Evidence for basal marine ice in the Filchner-Ronne Ice Shelf, Nature, 358, 399–401.

Orsi, AH, T Whitworth, WD Nowlin (1995) On the meridional extent and fronts of the Antarctic Circumpolar Current, Deep-Sea Research I, Vol. 42, No. 5: 64-673

Padman, L., H. A. Fricker, R. Coleman, S. Howard, and L. Erofeeva (2002), A new tide model for the Antarctic ice shelves and seas, Ann. Glaciol., 34(1), 247–254.

Paterson W. S. B. (1994), The physics of glaciers, third edition, Oxford, Butterworth-Heinemann, 481 p.

Pattyn F and D Derauw (2002) Ice-dynamic conditions of Shirase Glacier, Antarctica, inferred from ERS SAR interferometry, J. Glaciol. 48 (163): 559-565

Pattyn, F, S De Brabander, A Huyghe (2005) Basal and thermal control mechanisms of the Ragnhild glaciers, East Antarctica. Annals of Glaciology 40: 225-231.

Pattyn, F. (2002a), Transient glacier response with a higher-order numerical ice-flow model, J. Glaciol., 48(162), 467–477.

Pattyn, F. (2002b), Ice-flow characteristics over a rough bedrock: Implications for ice-core interpretation, Polar Meteorol. Glaciol., 16, 42–52.

Pattyn, F. (2003), A new 3D higher-order thermomechanical ice-sheet model: Basic sensitivity, ice-stream development and ice flow across subglacial lakes, J. Geophys. Res., 108(B8), 2382, doi:10.1029/2002JB002329.

Pattyn, F. (2010), Antarctic subglacial conditions inferred from a hybrid ice sheet/ice stream model, Earth Planet. Sci. Lett., 295, 451–461.

Pattyn, F., A. Huyghe, S. De Brabander, and B. De Smedt (2006), Role of transition zones in marine ice sheet dynamics, J. Geophys. Res., 111, F02004, doi:10.1029/2005JF000394.

Pattyn, F., et al. (2012), Melting and refreezing beneath Roi Baudouin Ice Shelf (East Antarctica) inferred from radar, GPS, and ice core data, J. Geophys. Res., 117(F4), F04008.

Pattyn, F., K. Matsuoka, and J. Berte (2010), Glacio-meteorological conditions in the vicinity of the Belgian Princess Elisabeth Station, Antarctica, Antarct. Sci., 22(1), 79–85.

Payne, A. J., P. R. Holland, A. P. Shepherd, I. C. Rutt, A. Jenkins, and I. Joughin (2007), Numerical modeling of ocean-ice interactions under Pine Island Bay's ice shelf, J. Geophys. Res., 112, C10019, doi:10.1029/2006JC003733.

Pettit, E. C., T. Thorsteinsson, H. P. Jacobson, and E. D. Waddington (2007), The role of crystal fabric in flow near an ice divide, J. Glaciol., 53, 277–288

Potter, J. R., and J. G. Paren (1985), Interaction between ice shelf and ocean in George VI Sound, Antarctica, in Antarctica, in Oceanology of the Antarctic Continental Shelf, Antarct. Res. Ser., vol. 43, edited by S. Jacobs, pp. 35–58, AGU, Washington, D. C., doi:10.1029/AR043p0035.

Pritchard, H. D., S. R. M. Ligtenberg, H. A. Fricker, D. G. Vaughan, M. R. van den Broeke, and L. Padman (2012), Antarctic ice-sheet loss driven by basal melting of ice shelves, Nature, 484, 502–505, doi:10.1038/nature10968.

R. C. A. Hindmarsh, E. C. King, R. Mulvaney, H F. J. Corr, G. Hiess and F. Gillet-Chaulet (2011) Flow at ice-divide triple junctions: 2. Three-dimensional views of isochrone architecture from ice-penetrating radar surveys. J. Geophys. Res. 116, F02024, doi:10.1029/2009JF001622.

Raymond, C. F. (1983), Deformation in the vicinity of ice divides, J. Glaciol., 29, 357–373.

Reeh, N. (1988), A flow-line model for calculating the surface profile and the velocity, strain-rate, and stress fields in an ice sheet, J. Glaciol., 34 (116), 46–54.

Rignot E. and Mac Ayeal D. R. (1998), Ice Shelf dynamics near the front of the Filchner-Ronne Ice Shelf, Antarctica, revealed by SAR interferometry, J. Glaciol., Vol. 44, 147, 405–418

Rignot, E. J. (1998), Fast recession of a West Antarctic glacier, Science, 281(5376), 549–551, doi:10.1126/science.281.5376.549.

Rignot, E. J., and S. S. Jacobs (2002), Rapid bottom melting widespread near Antarctic ice sheet grounding lines, Science, 296(5575), 2020–2023.

Rignot, E. J., J. L. Bamber, M. R. van den Broeke, C. Davis, Y. Li, W. J. van de Berg, and E. van Meijgaard (2008), Recent Antarctic ice mass loss from radar interferometry and regional climate modelling, Nat. Geosci., 1, 106–110.

Rignot, E., J. Mouginot, and B. Scheuchl (2011), Ice flow of the Antarctic Ice Sheet, Science, 333(6048), 1427–1430, doi:10.1126/science.1208336.

Rippin, D. M., et al. (2003), Basal topography and ice flow in the Bailey/Slessor region of East Antarctica, Journal of Geophysical Research-Earth Surface, 108(F1).

Roberson, S. and B. Hubbard 2010. Application of borehole optical televiewing to investigating the 3-D structure of glaciers: implications for the formation of longitudinal debris ridges, midre Lovenbreen, Svalbard. *Journal of Glaciology*, **56**(195): 143-156.

Russell-Head D. S. and Wilson C. J. L. (2001), Automated fabric analyser system for quartz and ice, Abstr. Geol. Soc. Aust., 64, 159.

Samyn D., Remy J.P., Duval P., Montagnat M. and Tison J.L. (2007), Compression experiments on marine ice from Nansen Ice Shelf, Antarctica: Implications for ice-shelf/continent interactions, Geophys. Res. Abstr., Vol. 9, 00803

Sarmiento J. L. and Gruber N. (2006), Ocean Biogeochemical Dynamics, Princeton University Press, 503 p.

Schoof, C. (2007), Ice sheet grounding line dynamics: Steady states, stability and hysteresis, J. Geophys. Res., 112, F03S28, doi:10.1029/2006JF000664.

Schulson E. M. and Duval P. (2009), Creep and Fracture of Ice, Cambridge University Press, first edition, 401p.

Shapiro, N. M., and M. H. Ritzwoller (2004), Inferring surface heat flux distributions guided by a global seismic model: particular application to Antarctica, Earth and Planetary Science Letters, 223(1-2), 213-224.

Shepherd, A., D. Wingham, and E. Rignot (2004), Warm ocean is eroding West Antarctic Ice Sheet, Geophys. Res. Lett., 31, L23402, doi:10.1029/2004GL021106.

Shibuya, K., K. Doi, and S. Aoki (1999), Precise determination of geoid height and free-air gravity anomaly at Syowa Station, Antarctica, Earth Planets Space, 51, 159–168.

Siegert, M. J., et al. (2004), Macro-scale bed roughness of the Siple Coast ice streams in West Antarctica, Earth Surface Processes and Landforms, 29(13), 1591-1596.

Smedsrud, L., A. Jenkins, D. M. Holland, and O. A. Nøst (2006), Modeling ocean processes below the Fimbul Ice Shelf, J. Geophys. Res., 111, C01007, doi:10.1029/2005JC002915.

Souchez, R., M. Meneghel, J. L. Tison, R. Lorrain, D. Ronveaux, C. Baroni, A. Lozei, I. Tobacco, and J. Jouzel (1991), Ice composition evidence of marine ice transfer along the bottom of a small ice shelf, Geophys. Res. Lett., 18(5), 849–852.

Steinhage, D., et al. (2001), Subglacial topography and internal structure of central and western Dronning Maud Land, Antarctica, determined from airborne radio echo sounding, Journal of Applied Geophysics, 47(3-4), 183-189.

Thoma, M., A. Jenkins, D. Holland, and S. Jacobs (2008), Modelling circumpolar deep water intrusions on the Amundsen Sea continental shelf, Antarctica, Geophys. Res. Lett., 35, L18602, doi:10.1029/2008GL034939.

Timmermann, R., et al. (2010), A consistent dataset of Antarctic ice sheet topography, cavity geometry, and global bathymetry, Earth Syst. Sci. Data, 3(2), 231–257, doi:10.5194/essdd-3-231-2010.

Tison J.L. and Khazendar A. (2001), A two phase approach to the simulation of the combined isotope/salinity signal of marine ice, J. Geophys. Res., vol. 106, C12, 31387–31401

Tison, J. L., and A. Khazendar (2001), The isotope/salinity relationship in marine ice: New perspectives, J. Geophys. Res., 106(C12), 31,387–31,401.

Tison, J. L., D. Ronveaux, and R. Lorrain (1993), Low salinity frazil ice generation at the base of a small Antarctic ice shelf, Antarct. Sci., 5(3), 309–322.

Tison, J. L., R. Lorrain, A. Bouzette, M. Dini, T. Bondesan, and M. Stiévenard (1998), Linking land fast sea ice variability to marine ice accretion at Hells Gate Ice Shelf, Ross Sea, in Antarctic Sea Ice Physical Processes, Interactions and Variablility, Antarct. Res. Ser., vol. 74, edited by M. Jeffries, pp. 375–407, AGU, Washington, D. C., doi:10.1029/AR074p0375.

Tison, J.-L., Ronveaux D. and Lorrain R. D.(1993) Low salinity frazil ice generation at the base of a small Antarctic ice shelf. Antarct. Sci., Vol. 5 3, 309–322

Treverrow A., Warner R. C., Budd W. F. and Craven M. (2010), Meteoric and marine ice crystal orientation fabrics from the Amery Ice Shelf, East Antarctica, J. Glaciol., Vol. 56, 199, 877–890

Trickett Y. L., Baker I. and Pradhan P. M. S. (2000), The effects of sulphuric acid on the mechanical properties of ice single crystals, J. Glaciol., Vol. 46, 153, 239–243(5)

van de Berg, W. J., M. R. van den Broeke, C. H. Reijmer, and E. van Meijgaard (2006), Reassessment of the Antarctic surface mass balance using calibrated output of a regional atmospheric climate model, J. Geophys. Res., 111, D11104, doi:10.1029/2005JD006495.

van de Berg, W.J., M.R. van den Broeke, C.H. Reijmer and E. van Meijgaard 2006. Reassessment of the Antarctic surface mass balance using calibrated output of a regional atmospheric climate model. *Journal of Geophysical Research*, **111**(D11): D11104.

Vaughan, D. G., H. F. J. Corr, C. S. M. Doake, and E. D. Waddington (1999), Distortion of isochronous layers in ice revealed by groundpenetrating radar, Nature, 398, 323–326.

Waddington, E. D., T. A. Neumann, M. R. Koutnik, H. P. Marshall, and D. L. Morse (2007), Inference of accumulation-rate patterns from deep layers in glaciers and ice sheets, J. Glaciol., 53(183), 694–712.

Weertman, J. (1974), Stability of the junction of an ice sheet and an ice shelf, J. Glaciol., 13, 3–11.

Weertman, J. (1983), Creep deformation of ice, Annu. Rev. Earth Planet. Sci., Vol. 11, 215 p.

Whitworth, T., A. H. Orsi, S. J. Kim, W. D. Nowlin, and R. A. Locarnini (1998), Water masses and mixing near the Antarctic slope front, in Ocean, Ice, and Atmosphere: Interactions at the Antarctic Continental Margin, Antarct. Res. Ser., vol. 75, edited by S. S. Jacobs and R. F. Weiss, pp. 1–27, AGU, Washington D.C., doi:10.1029/AR075p0001.

Wilson C.J.L., Russell-Head D.S. and Sim H.M. (2003), The application of an automated fabric analyser system to the textural evolution of folded ice layers in shear zones, Ann. Glaciol., Vol. 37, 7–17

Zotikov I. A. (1986), The thermophysics of glaciers, Glaciol. Quaternary Geol., 275 p

ANNEX 1: COPY OF THE PUBLICATIONS

The annexes are available on the website

https://www.belspo.be/belspo/fedra/prog.asp?l=en&COD=EA